

Experimental characterization and finite element validation of orthotropic 3D-printed polymeric parts

*Original*

Experimental characterization and finite element validation of orthotropic 3D-printed polymeric parts / Torre, Roberto; Brischetto, Salvatore. - In: INTERNATIONAL JOURNAL OF MECHANICAL SCIENCES. - ISSN 0020-7403. - 219:1 April 2022 (107095)(2022), pp. 1-18. [10.1016/j.ijmecsci.2022.107095]

*Availability:*

This version is available at: 11583/2955150 since: 2022-02-14T13:13:36Z

*Publisher:*

Elsevier

*Published*

DOI:10.1016/j.ijmecsci.2022.107095

*Terms of use:*

This article is made available under terms and conditions as specified in the corresponding bibliographic description in the repository

*Publisher copyright*

Elsevier preprint/submitted version

Preprint (submitted version) of an article published in INTERNATIONAL JOURNAL OF MECHANICAL SCIENCES © 2022, <http://doi.org/10.1016/j.ijmecsci.2022.107095>

(Article begins on next page)

# Experimental characterization and finite element validation of orthotropic 3D-printed polymeric parts

Roberto Torre\* and Salvatore Brischetto †

Department of Mechanical and Aerospace Engineering, Politecnico di Torino, Torino, Italy

**Abstract** Components fabricated via Fused Filament Fabrication (FFF) have an anisotropic response, which is further complicated by an intra-part and a part-to-part variation of their mechanical properties. In addition, the mechanical characterization and analysis process has not been standardized yet, making it difficult to assess the structural behavior and verify the compliance of a part with the performance criteria in service. This paper intends to fill this gap for specific printing process parameters. First, it speculates that a linear infill with a 100% infill could help to reduce the anisotropy of the parts to a mild orthotropy. Thin components have provided a quick and preliminary confirmation of the approach. After an initial test setup design, which was required to standardize the method, the in-plane behavior was studied. Classical dog-bone specimens returned unsatisfactory results when coupled with the internal structures. As a result, the paper takes inspiration from the test methods for Uni-Directional Composites (UDCs). It uses sets of Design of Experiments (DoEs) to determine the optimal shape of the tabs. This method managed to quantify the factors of the  $3 \times 3$  reduced elastic coefficients matrix. Finally, the paper presents a set of three-point bending, simple bending, and bending-torsion tests on samples featuring different laminations. 2D FE models tuned with the experimental properties simulated them, following the Classical Lamination Theory (CLT) approach. For consistency, a shear penalization was introduced for the out-of-plane shear. The FE models delivered an excellent mechanical response prediction; this result appears to validate the approach and the method and endorses 2D FEM and CLT as reliable tools to analyze linear infill FFF parts.

**Keywords:** fused filament fabrication; mechanical characterization; PLA; experimental campaign; classical lamination theory; constitutive model; orthotropic materials.

## 1 Introduction

Shaping materials into components follows five basic principles [1]. *Subtractive technologies* start from a block of raw material, use tools to remove the excess, and give the component the intended shape. *Transformative* (or forming) *shaping* refers to a change in a shape obtained applying a force. Welding and sawing give an example of *joining and dividing technologies*, respectively. Finally, *additive shaping* consists of continuous addition of material, usually following a layer-by-layer approach [2]. *Additive Manufacturing* (AM), or *3D printing*, defines a specific *production process category*. ISO ASTM 52900 standard recently established names, definitions, and vocabulary associated with those new approaches

---

\*e.mail: roberto.torre@polito.it.

†Author for Correspondence: Salvatore Brischetto, Department of Mechanical and Aerospace Engineering, Politecnico di Torino, Corso Duca degli Abruzzi 24, 10129 Torino, ITALY. e.mail: salvatore.brischetto@polito.it.

[3]. It gives a preliminary listing of those processes as a function of the material type. Further and more detailed catalogs consider the feedstock, how the material is distributed and processed. Wong and Hernandez [2] also proposed a classification in terms of the *state* of the raw material, either powder, liquid, or solid. The concepts of *material distribution* and the *layer-by-layer approach* go parallel and are the foundation of these processes. A computer procedure slices the 3D geometry of the element to print into a user-defined number of layers. Their shape is physically accomplished by adding material to the previous step. Such an approach allows a rapid transition between design and production; even a complex shape comes through a standardized process of material superposition. Designing any specific tool, support, or mold is not necessary to prepare the production. The impact of reducing overall production times is evident, especially from prototyping [4], small-scale, and customized productions [5].

Different materials imply other principles of *fusion*, *addition*, and *bonding*. This paper focuses on Fused Filament Fabrication (FFF), also known as Fused Deposition Modelling [6]. It processes thermoplastics in a solid filament; ABS, PLA, PC, PET, PEEK, and ULTEM are some examples. A *gear wheel* drags the filament and pushes it towards the *hot end*, a heated chamber featuring a metallic nozzle. In a specific temperature range, the filament liquifies and is pushed out of the nozzle [7]. Simultaneously, the nozzle moves by keeping a constant distance, the *layer height*, from a flat surface. The first layer is deposited on the *printing bed* of the device; the others rely on the previous deposition [8]. The thread has a cylindrical shape outside the nozzle. The layer height is smaller than the nozzle diameter [9]; this flattens the thread, which takes the form of a filament with an oval eyelet cross-section and develops in length due to the simultaneous motion of the nozzle. It is a numerically controlled process governed by the printing strategy and by the shape of the printed layer. Over the same layer, the filaments can be deposited following a customizable infill strategy and infill percentage. The *linear infill* is the simplest; fibers are deposited in parallel, adjacent to each other when a 100% infill percentage is chosen. As soon as a layer is complete, the printing bed moves down a layer height, and new filaments are deposited over it. For each layer, the operator can set a defined number of peripheral filaments, closely following the external and internal profile of the area. For some of those parameters, a set of recommended ranges exist for different materials; however, a trial-and-error process together with the experience of the operator are essential components.

An almost direct shift from the design phase to the production is the leading advantage of AM, even when parts have complex inner shapes. This is the case of aerospace applications [10], which demand lightweight structures in addition [11]. Polymers processed via FFF are not foreign to aerospace applications [12]; the literature reports application examples specifically in the Unmanned Aerial Vehicle (UAV) context. Bigger applications require shifting to metal AM [13]. Improving the mechanical performances is possible by switching to reinforced thermoplastics; 3D-printed carbon fiber-reinforced plastics give example [14–16]. The ongoing problem is that of mechanical design and validation. The mechanical properties, the surface finish, and the dimensional accuracy are a function of the processing parameters [17]; the software used for toolpath generation also affects their performances [18]. 3D printed initially targeted the prototyping, proposing as an easy and rapid-to-use tool. However, manufacturing final components require evaluating compliance with the performance criteria. Overlapping layers induce an overall directionality in the mechanical properties [19, 20], which combines with the component orientation into the printer reference system. Furthermore, the machine and the printing parameters affect the part properties. This theme still features much uncertainty [21]: it goes beyond quantifying the mechanical properties but implies understanding how components perform and behave. The literature shows two main threads of investigation: *determining how* specific process parameters affect the structural behavior of the parts and *quantifying some* mechanical properties under particular process parameters. Predicting the mechanical behavior of FFF components by exploiting the characterization campaigns received less attention. Some authors used the mechanical properties of the feedstock materials to predict it [22], even if the literature shows they significantly differ from those of the finished parts [23–25].

Among the first, Rodriguez et al. [23] tackled the issue. They quantified the modulus of elasticity and the shear modulus of an ABS filament and compared it to the tensile tests on printed specimens, following ASTM D3039. They verified the mechanical properties reduction from the feedstock material to the finished component, as high as 37% (for modulus) and 57% (for strength). The authors investigated the directionality in the mechanical properties of the parts: they studied the in-plane behavior only (e.g., all the specimens printed flat-wise) but with different filaments orientations, showing an off-axis angle influence. They speculated that voids distribution and the loss of molecular chains orientation might have played a role in this. Still, it did not fully justify the phenomenon. Among the first, they defined a material reference system with direction 1 coinciding with the filaments and direction 2 normal to them. Later, Ahn et al. [24] compared 3D-printed specimens and molded coupons, focusing on tensile and compressive strengths. They found a tensile strength as low as 35% and compressive strength as low as 20% with the same feedstock material. They identified the influence of several process parameters on the mechanical response: the raster angle and the air gap appeared to be crucial. Furthermore, they qualified specimens with a rectangular and constant cross-section: dog-bone samples lead to stress concentration inducing premature failures. More recently, Lay et al. [25] focused on three polymers, ABS, PLA, and Nylon, and investigated the tensile strength, tensile modulus, and impact resistance. Again, they found remarkable differences between the injection molded and 3D-printed coupons. The percentages can be as high as 48% for the tensile strength and 50% for the Young modulus. However, such behavior depends on the specific plastic. The authors used generic dumbbell specimens for tensile testings, not discussing their actual dimensions and shape; they gave no information regarding the failure location, which is helpful to select acceptable failure modes. The specimens grow flatwise, with an alternated  $[0^\circ/90^\circ]$  raster orientation. Another example is provided by the work of Zaldivar et al. [26]. The authors built dog-bone coupons to evaluate the tensile modulus and strength of 3D-printed ULTEM. They confirmed the previous results but observed dependence on sample orientation. Depending on this parameter, the reduction in tensile strength ranged between 15% and 56%. The authors printed six ASTM D638 type III samples with the same infill but different positioning and orientation in the printing volume; this modified their settlement to the load application direction. The DIC monitoring of the strain field revealed some localized strain concentrations, some of them close to the transition region between the gripping and the gauge areas. Gebisa et al. [27] also worked on ULTEM. The authors switched to constant cross-section specimens per ASTM D3039 to avoid the stress concentration issue of dog-bone specimens. They proposed five factors, two levels, Design of Experiment (DoE), to analyze the impact of the air gap, raster width, raster angle, contour number, and contour width on tensile strength. They confirmed that the raster angle affects strength under the same specimen orientation. The tensile strength of ULTEM can be as low as 30 MPa or as high as 87 MPa, depending on it. All the other parameters appeared to be less critical. Durgun et al. [28] already had performed an analogous investigation on ABS. They combined three parts orientations and five different raster angles to build tensile specimens, aiming to observe their influence on the elastic modulus, tensile strength, and surface roughness. They confirmed the importance of these parameters, highlighting the considerable weight of the part orientation: the parts built in the vertical direction performed worse than the others. There is a large variability in tensile strengths; fewer fluctuations arose in tensile modulus. However, the best tensile properties emerged along with the deposition direction within the same part orientation. In this research, the authors produced dog-bone specimens following ISO 527: many coupons failed close to the filleted region. SEM analysis justified the failure modes with specimen mesostructure and orientation to the load application direction. However, the mutual influence between the geometry and the mesostructure, which could have induced a premature failure, was not discussed.

Several authors studied the influence of many process parameters other than the raster angle. For example, Wittbrodt [29] assessed the extrusion temperature and even the color additive; both appeared to influence the crystallinity and, consequently, the tensile strength. Similarly, Pu [30] deepened the influence of crystallinity on the mechanical properties of 3D-printed PEEK, linking it with the process

parameters. Tymrak [31] discussed the impact of the layer thickness and two linear infills. The author confirmed a mild decay of the mechanical properties from injection-molded values. Uddin [32] also evaluated the impact of the layer thickness, together with specimen arrangement on the printer volume. He confirmed the anisotropic behavior of FFF-produced elements. A 4-parameter, two-level Design of Experiment allowed Griffiths [33] to evaluate the impact of specimen orientation, the number of peripheral filaments, fill percentage, and layer height. The higher the infill percentage and the number of perimeters, the better the outputs, using the tensile stiffness and strength as output parameters. Sukindar [34] confirmed the positive effect of peripheral filaments, which are no more than filaments distributed along with the longitudinal direction of the specimen; this point needs to undergo serious consideration, as their contribution might hide the infill behavior [35]. Rodriguez [36] confirmed that high internal infill percentages improve the mechanical properties and verified that the layer height slightly affects them. Several authors discussed the influence of the quantity and distribution of porous defects. In [37], negative air gaps between adjacent filaments reduced porosity, thus increasing the mechanical performances. Similar results are discussed in [38, 39]. Tang et al. [40] also demonstrated the influence of the printing temperature and the printing speed, even with lattice structures. PLA reached a maximum tensile modulus and strength at  $230^{\circ}\text{C}$ , and improved properties with higher printing speeds. The influence of the printing temperature and speed on PLA was also noted by Tang et al. [40] while studying the fracture toughness of FFF 3D printed and sintered parts. Those two process parameters reduce the bearing capacity and the initial crack opening as their values increase.

Dizon et al. [41] underlined the lack of standardized test methods in AM. Narrowing to FFF, most research relies on existing ISO/ASTM standards. ASTM D638, standardizing the tensile properties determination in plastics, has been proposed in several works. Other researchers questioned whether they were adequate. The premature failures reported in [24, 42] did not occur in every experimental campaign because it depends on the infill-geometry interaction, which changes if printing parameters are modified. Some authors followed ASTM D3039, which standardizes tensile properties determination in composite materials, relying on rectangular cross-section coupons. This inconsistency leads to heterogeneous results: Torrado [43], and Laureto [44] found a significant difference in tensile strengths with different specimens. Torrado compared ASTM D638 type I, type IV, and type V specimens and suggested the need for specific mechanical testing standards involving multiple test geometries. The ultimate tensile strength varied up to 10% between them. The authors also demonstrated a similarity in fracture behavior and ultimate tensile strength between vertical specimens and horizontal coupons with transverse filaments, proposing the latter as an easier surrogate. Laureto et al. limited their study to ASTM D638 type I and type IV specimens. However, they performed an extensive experimental campaign based on more than 400 coupons and 47 different printers; type IV specimens might overestimate the ultimate tensile strength of type I coupons. This observation suggests checking that the geometry of the tensile specimens matches that of the printing component to rely on relevant values. Different specimen geometries with other mechanical properties suggest a part-to-part variation; furthermore, other mechanical properties found in specimens with different positions and orientations suggest an intra-part variation. These points restrict using FFF in functional parts [45]: the absence of standardized procedures for mechanical characterization is a limit for broad application of AM. Globally accepted standards on test methods are urgently needed: parts qualification is impossible, which precludes further market opportunities. Leveraging on them will increase process and machines reliability.

Quantifying the performances could still be overcome with a characterization campaign performed after defining the printer, the plastic, and the parameters. However, layer-by-layer processing, raster angle, element orientation, and void pattern still play a crucial role, inducing an anisotropy, as high as 50% [46]. The bonding between adjacent and superposed filaments is the leading cause, involving a significant anisotropy. The more the process parameters reflect on their characteristics, the more evident the anisotropy. Moreover, the mechanical properties in compression may significantly differ

from those in tension [47, 48]. All those aspects require investigation to support the production of functional parts [49]. Even if all the manufacturing parameters, the raw material, and the printer have been defined and a characterization campaign run, the mechanical properties would still be a function of the coupon orientation and shape. This paper targets defining a constitutive model of the printed material, through which the structural analysis gets reliable results.

## 1.1 Macro-mechanical approach to the problem

This paper considers a macromechanical approach: by leaving out the behavior at the local level, it seeks a constitutive model of homogeneous equivalent material. A sequence of layers featuring a characteristic pattern is questionable to show a mechanical behavior like a homogeneous melting. Designing a standardization process requires relating the material properties to its mesostructure. However, the mesostructure depends on the coupon geometry and the printing parameters. Different filling strategies lead to different mesostructures, resulting in other mechanical behavior due to varying degrees of anisotropy. If framed on the 100% linear infill, the problem becomes simpler: filaments are adjacent and parallel inside each layer. Nothing changes from layer to layer: symmetries exist, and the mechanical properties might manifest some directionality, reflecting on special features along with three perpendicular directions. *Direction 1*, running parallel to the filaments; *direction 2*, orthogonal to filaments and parallel to layers; *direction 3*, orthogonal to filaments and layers. Those three form three planes of geometric symmetry: *plane 1 – 2*, parallel to filaments and layers; *plane 1 – 3*, parallel to filaments and orthogonal to layers; *plane 2 – 3*, orthogonal to filaments and layers.

A geometrical analogy with UDC exists; they show the same symmetries, implying an orthotropic behavior. A clue comes from the difference in the mechanical properties along with the three directions [50–52]. In analogy to UDCs, direction 1 shows the highest mechanical properties; filaments could support the applied load as fibers do. However, there is no matrix responsible for load transmission: *intra-layer bonds* appear between adjacent filaments of the same layer; *inter-layer bonds* arise between superposed filaments of different layers. Moreover, the contact surfaces differ: when a filament develops next to the previous one, the first is still at moderate temperature due to the short elapsed time. A longer time may have elapsed when considering superposed filaments. Different cooling rates occur [53], and they take fundamental importance. Despite this, at the macromechanical level, the analogy may still hold. If confirmed, it would indicate that the mechanical behavior of FFF 3D-printed components is orthotropic under specific circumstances. A tailored mechanical characterization campaign is required, with experimental tests fitting the orthotropy hypothesis. Six mechanical characterization tests would be needed: three tensile tests to quantify the three Young moduli and the three Poisson ratios; three shear tests to complete the diagonal of the matrix. The first evaluation of this approach comes from an intermediate and simplified step. In composite materials, the mechanical behavior of a laminate can be studied through the Classical Lamination Theory (CLT), having the mechanical properties of each lamina, its thickness, and orientation defined. Extending the simplifying hypotheses of CLT to FFF components, one would read:

- each layer is thin enough;
- macroscopically, each layer consists of a linear-elastic, orthotropic, and homogeneous material;
- both the layers and the structure undergo two-dimensional plane stress;
- an ideal bond exists between layers;
- the structure fulfills the Kirchhoff hypothesis.

In the material reference system, the CLT assumptions reduce the matrix of the elastic coefficients to

$$\mathbf{Q} = \begin{bmatrix} Q_{11} & Q_{12} & 0 \\ Q_{12} & Q_{22} & 0 \\ 0 & 0 & Q_{66} \end{bmatrix} \quad (1)$$

where

$$Q_{11} = \frac{E_1^2}{E_1 - \nu_{12}^2 E_2}, \quad Q_{12} = \frac{\nu_{12} E_1 E_2}{E_1 - \nu_{12}^2 E_2}, \quad Q_{22} = \frac{E_1 E_2}{E_{11} - \nu_{12}^2 E_2}, \quad Q_{66} = G_{12} \quad (2)$$

$E_1$  and  $E_2$  are the Young moduli of directions 1 and 2, respectively;  $G_{12}$  is the shear modulus, and  $\nu_{12}$  the Poisson ratio between directions 1 and 2. The definitions already consider the relationship between the Poisson ratios with reversed indices. Layers whose filaments have a raster angle  $\theta$  other than  $0^\circ$  (structure reference system not coinciding with the material one) require the following transformation:

$$\mathbf{Q}^s = \mathbf{T}^{-1} \mathbf{Q} \mathbf{T} \quad (3)$$

where  $s$  identifies the structure reference system and

$$\mathbf{T} = \begin{bmatrix} \cos^2(\theta) & \sin^2(\theta) & 2\cos(\theta)\sin(\theta) \\ \sin^2(\theta) & \cos^2(\theta) & -2\cos(\theta)\sin(\theta) \\ -\cos(\theta)\sin(\theta) & \cos(\theta)\sin(\theta) & \cos^2(\theta) - \sin^2(\theta) \end{bmatrix} \quad (4)$$

Four parameters, plus the raster angle  $\theta$ , describe the mechanical behavior of an orthotropic layer.

Those assumptions seem to be confirmed by previous works. The pioneering work of Rodriguez et al. [23] discussed about the two Young moduli  $E_1$  and  $E_2$ , the Poisson ratio  $\nu_{12}$ , and the shear modulus  $G_{12}$ . Their work relied on composites-like specimens and provided valuable insights on the orthotropic behavior of 3D-printed ABS. Nevertheless, no practical applications were suggested. Li et al. [54] expanded the approach to P400 filament and studied the polymeric layers as unidirectional composite laminae. The constitutive model considered an in-plane stress state and relied on the  $3 \times 3$  matrix of reduced elastic coefficients, a function of  $E_1$ ,  $E_2$ ,  $\nu_{12}$ , and  $G_{12}$ , rotated in case of raster angles other than  $0^\circ$  or  $90^\circ$ . The authors applied CLT to thin FFF-parts and tried to predict the coefficients through the mixture rule. Using the mechanical properties of the base polymer as a starting point,  $E_1$  derives from the longitudinal density of voids;  $E_2$  depends on a further empiric factor for bond strength in addition to the transverse density of voids. The same applies to the shear modulus  $G_{12}$ . The authors then compared the mechanical properties prediction with unidirectional and orthogonal ply specimens, following ASTM D3039. The in-plane shear modulus prediction was excellent; higher differences arose in the longitudinal direction (up to 11%) and the transverse direction (up to 5%). Surprisingly, the predictions on orthogonal-ply coupons revealed good results, with differences ranging between 2.4 and 7.1%. Such an approach was not further explored until the work of Casavola et al. [55]. They described the mechanical behavior of FFF polymers through CLT. The authors experimentally measured the elastic coefficients on ABS and PLA through ASTM D638 type I specimens: coupons with longitudinal filaments for  $E_1$  and  $\nu_{12}$ ; coupons with transversal filaments for  $E_2$ . The in-plane shear properties determination followed ASTM D3518: rectangular parts with constant cross-section and a stacking sequence of  $[+45^\circ / -45^\circ]$  for  $G_{12}$ . Although the authors modified the infill strategy following the mechanical properties under investigation, they kept a pair of peripheral beads in each coupon, always parallel to its longitudinal axis; they did not deepen the heterogeneity of coupon geometries. The results endorsed the 3D-printed parts orthotropy, more pronounced for ABS ( $E_1 = 1.81$  GPa vs.  $E_2 = 1.15$  GPa) than for PLA ( $E_1 = 3.12$  GPa vs.  $E_2 = 2.77$  GPa). The authors verified the capability of CLT in predicting the behavior of ABS and PLA specimens by simulating and then testing tensile specimens with a  $[+30^\circ / -30^\circ / 0^\circ / -30^\circ / +30^\circ]$  symmetrically balanced stacking sequence. The comparison gave promising results in terms of elastic moduli: CLT predicted 1.88 GPa for ABS and 3.27 GPa for PLA; the experimental campaign returned 1.86 GPa and 3.35 GPa, respectively.

More recently, Yap et al. studied the orthotropy of Acrylonitrile Styrene Acrylate (ASA) [56] and Polycarbonate-Acrylonitrile butadiene styrene (PC-ABS) [57]. They proposed a non-destructive ultrasonic methodology for characterizing the material and defined the  $6 \times 6$  matrices of elastic coefficients through a cubic and oblique specimen set. Then, the authors performed a set of classical tensile tests in the three principal material directions to (partially) confirm the previous results. The comparison between the three principal elastic moduli showed pronounced differences, as the ultrasonic-tested specimens seemed to have a stiffer behavior. The authors performed a three-point plus four-point bending test and a four-point bending test plus an impact hammer test to verify the mechanical properties using  $[+45^\circ / -45^\circ]$  coupons. A graphical comparison of the Force vs. Displacement relations of bending tests revealed an excellent agreement of the experimental results with FE models of the tests. Hammer tests revealed deviations lower than 3% in the first three frequencies. Those two works are significant as they further confirmed the orthotropy in components with a linear infill and validated ultrasonic tests for a fully elastic properties determination in 3D-printed parts.

Getting back to in-plane properties determination, Saeed et al. [58] applied the CLT approach on 3D printed plastics reinforced through carbon fibers. They determined  $E_1$ ,  $E_2$  and  $G_{12}$  through ASTM D3039 coupons. They predicted these quantities through CLT and found the results in agreement: the Young modulus in the longitudinal direction practically coincided (73.20 GPa vs. 72.87 GPa); a more significant gap arose in the shear modulus (2.23 GPa vs. 3.43 GPa). Goh et al. [16] still worked on continuous carbon fiber reinforced 3D printed polymers. They applied the standardized test methods for unidirectional tensile (ASTM D3039), compression (ASTM D6641), and shear (ASTM D6641) properties determination, relying on the stiffer and stronger behavior of long fibers, representing the critical effect in the principal material direction coinciding with the deposition one. The  $6 \times 6$  matrix of elastic coefficients determined thereby allowed them to propose a 3D FE model of a UAV component and discuss an effective topological optimization.

The orthotropy hypothesis has been found promising in all the previous researches. Some of them determined a set of in-plane mechanical properties but failed to validate their capability in predicting the response of components under effective loading conditions. On the other hand, more recent researches quantified all the coefficients of orthotropic 3D printed polymers and even validated them through experimental-numerical tests. Nevertheless, the theme of standardizing the tests and, in particular, the classical ones for tensile/shear properties determination remained unsolved. The literature research showed a remarkable amount of heterogeneity in this regard. Additionally, the literature still missed such a process of mechanical properties determination and following validation for PLA. This paper aims to fill these gaps and consolidate the mechanical characterization approach to 3D printed polymers: the boundaries of the tests and the characteristics of polymeric coupons are studied through a set of Designs of Experiments. Their outcomes and the orthotropy hypotheses receive definitive validation through different experimental tests coupled with FE models. In doing so, the paper introduces the CLT approach, which, once finally validated and under defined assumptions, strongly limits the properties to determine, thus simplifying the practical implications of the results.

## 2 Experimental program and procedure

This simplified approach allows designing an experimental campaign with a view to the  $3 \times 3$  reduced elastic coefficients matrix only, which implies determining  $E_{11}$  and  $E_{22}$ ,  $\nu_{12}$ , and  $G_{12}$ , and translates into determining the in-plane mechanical properties of 3D printed polymers via two tensile tests and a shear test. The setup of the experimental campaign, however, requires investigation. No published standards exist for the mechanical characterization of 3D printed polymers through this approach. Sacrificial spools have been used in a preliminary experimental campaign to design the tests. In this way, a single and dedicated spool has been kept for the actual characterization and validation tests, maintaining consistency between them.

Mechanical/Physical properties		
Density	1.24 g/cm <sup>2</sup>	ASTM D792
Tensile strength	65 MPa	ASTM D638
Tensile yield	60 MPa	ASTM D638
Young modulus	3950 MPa	ASTM D638
Impact strength	5.5 KJ/m <sup>2</sup>	ASTM D256
Moisture absorption	< 1%	ISO 61
Thermal properties		
Printing temperature	195 – 215 °C	-
Melting temperature	150 °C	ASTM D3418
Vicat softening temp.	55 °C	ASTM D3418
Glass transition temp.	55 °C	ASTM D3418

Table 1: Data-sheet of the black PLA manufactured by Shenzhen Eryone Technology Co., Ltd. In the third column, the table reports the standards used to quantify the properties. [59].

Poly(lactic acid) (PLA) has been identified as the target material, given its wide use in several engineering applications [60]. A black PLA spool manufactured by Shenzhen Eryone Technology Co., Ltd. has been used. Table 1 reports the data-sheet provided by the manufacturer. All the specimens have been produced through a professional, industrial-grade, FUNMAT HT 3D printer set with the printing parameters reported in Table 2. The experimental setup is rich and multifaceted; this section serves as a map to facilitate understanding and contains the information common to all tests. The Young moduli and the Poisson ratio require two tensile tests. Hence, the problem demanded first to select the mesostructure of the specimens. As for the shape, attempting to resort to ASTM D638 the dog-bone geometry revealed its incompatibility with the mesostructures. For this reason, Section 3.2 addresses how to adapt UDCs specimen geometry and determines the characteristics of the gripping tabs through a set of Design of Experiments. In the end, it proposes the results of the tensile characterization campaign with the identified geometry. As for the shear modulus, the positive feedback offered by the tensile tests on specimens with UDCs geometry paved the way. An in-plane shear test was performed, relying on a tensile test with a specific mesostructure. Similarly, Section 4 addresses how to adapt the geometry, determines the characteristics of the gripping tabs through a set of DoEs, and proposes the results of the shear characterization campaign with the identified geometry. Finally, Section 5 validates the approach by presenting a comparison between the experimental and the numerically predicted behavior of thin specimens subjected to three-point bending and bending/bending-torsion tests.

## 2.1 Characterization tests procedure and calculation

In tensile and in-plane shear tests, the grips of the testing machine act on the top and bottom endpoints of the coupons. The machine is operated in displacement control, thus adapting the imposed load to meet the required displacement. These two physical quantities are sampled at 5 Hz and constitute a raw data set. The load acts in the longitudinal direction of the specimen and is therefore perpendicular to its cross-section. In tensile tests, the response of the material is studied in terms of tensile stress and longitudinal/transverse strain. By introducing the external load  $P$  and the initial cross-section of the region of interest  $A_0$ , the tensile stress can be calculated through Equation 5:

$$\sigma = \frac{P}{A_0} \quad (5)$$

In in-plane shear tests, the response of the material is studied in terms of shear stress and shear strain. As in tensile tests, the shear stress can be calculated through the applied load; exploiting the laminate

1st layer height	0.20	mm
Gen. layer height	0.10	mm
Nozzle diameter	0.40	mm
Extrusion width	0.50	mm
Infill percentage	100%	-
1st layer extrusion temp.	190	°C
Extrusion temperature	200	°C
Bed temperature	30	°C
Extrusion multiplier	1.05	-
Default speed	3000	mm/min
Retraction distance	3	mm

Table 2: FFF printing parameters used in producing the coupons; it is valid for all the tensile, in-plane shear, and validation specimens.

plate theory, it holds:

$$\tau_{12} = \frac{P}{2A_0} \quad (6)$$

Before each test, the dimensions of each specimen cross-section have been assessed by evaluating five times the thickness and the width and then averaging them to have typical values. The longitudinal and the transverse strains monitoring is needed in both tensile and in-plane shear tests. In the first case, these strains directly enter in the calculation of the tensile properties of the material; in the second case, they are combined to obtain the in-plane shear strain:

$$\gamma_{12} = \epsilon_x - \epsilon_y \quad (7)$$

where  $\epsilon_x$  is the longitudinal strain while  $\epsilon_y$  is the transverse strain. Measuring the longitudinal and the transverse strain is a task accomplishable through several contact and non-contact transducers. In previous work [61], the authors have experimentally measured that even a strain gauge designed explicitly for low modulus materials can induce a local reinforcing effect of the order of magnitude of 2%. This result is well documented in the literature and supported by the analytical models proposed by Beatty [62] and Ajovalasit [63]. For this reason, the research relied on a simple Digital Image Correlation (DIC) setup. Such a choice, supported by previous researchers [26,40], allows maintaining consistency, even between different tests, as the validation tests required evaluating the effects induced by the boundary conditions in terms of displacements. All the tests have been recorded with a Canon D3500 DSLR Camera with Nikkor 18-55mm f/3.5-5.6G DX VR AF-P optics. The DSLR camera frame rate has been reduced to 5 fps while importing the frames to the correlation software to match the sampling frequency of the testing machine. The focal distance has been set to 35 mm to avoid image distortions [64]. A random distribution of white/gray marks has been used to prepare the front surface of each specimen, increasing the image contrast. After each tensile / in-plane shear test, the machine stress vs. time relation (from the MTS testing machine) and the longitudinal/transverse strains vs. time relations (from DIC) must be synced over time. The following criterion has been applied. As the DSLR camera is manually operated, each video starts before the test beginning. The DIC shows a random displacement distribution in the first seconds due to image noise; the alignment of the longitudinal displacement map to the load application direction reports the test has begun. Syncing this with the MTS data is easy as the testing machine starts sampling as the test begins.

The characterization tests allowed calculating the *tensile/in-plane shear stiffness moduli* of the specimens via a set of consecutive regressions on stress-strain intervals of progressively rising size. The algorithm stopped iterating when a new coefficient differed by more than 5% from the mean of the

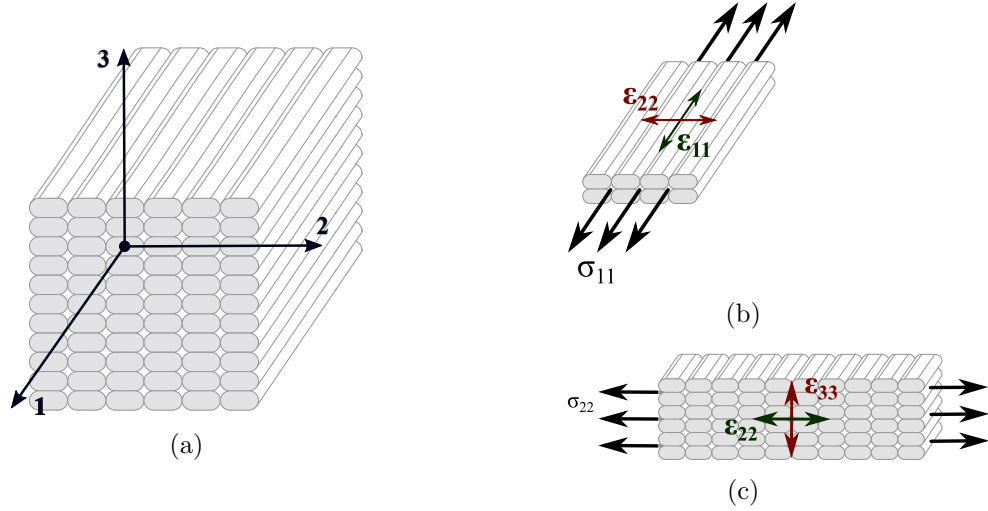


Figure 1: Mesostructure of FFF-printed parts with a unidirectional and 100% infill. A generic component with a cubic shape is shown in (a); (b) and (c) show the mesostructures of the specimen for tensile properties evaluation along with directions 1 and 2, respectively, in the material reference system.

previously calculated moduli; the stress at which the algorithm calculation stopped is recognized as the *tensile proportional limits*. The maximum load sampled by the testing machine is used to evaluate the *tensile/in-plane shear strength*, through the actual cross-section dimensions of the specimens. In tensile tests only, the algorithm evaluated the *Poisson ratio*, evaluating the average of the transverse strain vs. longitudinal strain ratio in the linear section of the curve. The correct alignment of the specimen with the load application direction is essential for the successful outcome of the test. Failing in this induces an eccentric load application responsible for lateral-lateral bending. All tensile and in-plane shear tests have been performed with the universal testing machine MTS QTest10; initial tests showed loads up to 5 kN for some specimens type; consequently, the testing machine was equipped with a 10 kN load cell. In addition, the alignment of the upper and lower jaws was verified before the campaign.

### 3 Tensile properties determination

This section is devoted to quantifying the tensile mechanical properties along with directions 1 and 2 in the material reference system. First, the mesostructural characteristics and the geometry of tensile specimens need to be deepened. This section deals with the issue of the coupons and their filaments orientations to the load application direction. After this, it validates specimen geometries providing a well-defined stress state such that the desired material properties can be obtained and unwanted side effects avoided.

Figure 1a proposes the mesostructure of a unidirectional FFF cubic element. The raster angle is the same for all the layers, which defines three principal material directions. Since each tensile test detects mechanical properties associated with the load application direction, it is necessary to visualize and extract coherently from the cube the specimens, or at least their region of interest. Figure 1b shows the mesostructure of a specimen for tensile properties evaluation along direction 1. The black arrows define the load application direction, which is parallel to direction 1 in the material reference system. The specimen lies flatwise, which allows determining the Young modulus  $E_{11}$  and the Poisson ratio  $\nu_{12}$ , monitoring the stress  $\sigma_{11}$  and the strain  $\epsilon_{11}$ , and matching the latter with the transverse strain  $\epsilon_{22}$ . Figure 1c proposes the mesostructure of a specimen for tensile properties evaluation along direction 2. It lies sidewise, which allows determining the Young modulus  $E_{22}$  and the Poisson ratio  $\nu_{23}$ , monitoring the stress  $\sigma_{22}$  and the strain  $\epsilon_{22}$ , and matching the latter with the transverse strain  $\epsilon_{33}$ .

The mesostructure of a specimen is not the only critical aspect; its geometry plays a key role. The geometries of tensile coupons are designed to produce an (almost) uniform tensile stress distribution inside the region of interest, higher in magnitude than any other specimen region. A failure in any different position suggests a stress concentration resulting from an incorrect introduction of the uniaxial load into the specimen, which prevents a correct evaluation of the tensile behavior. Due to the coexistence of the gripping pressure and the axial load, the gripping regions are characterized by a complex stress field. Higher cross-sections are usually designed to prevent the specimen from failing prematurely in those areas. Usually, polymers are tested with flat *dog-bone-shaped* coupons with a rectangular cross-section. The cross-section dimensions increase in the gripping area, where specimens are provided with expansions. In this case, the increase in cross-section area is achieved through width-tapering. Instead, composite materials use flat rectangular coupons with a constant cross-section. When needed, the expansions in the gripping regions are obtained through a set of customized *tabs* bonded to the specimen. In this case, the increase in cross-section area is achieved through thickness-tapering. As no standardized guidelines are available for 3D-printed plastics, reference will be made to standardized tests for properties determination in polymers in the first instance. A benchmark to assess if a tensile test is acceptable or not is the failure mode/location. The failure mode of those specimens will lead to propose and discuss modified UDC specimens-like.

### 3.1 Preliminary tests under ASTM D638 guidelines

A set of preliminary tests has been conducted to highlight if the set-ups following ASTM D638 are acceptable or not. At this stage, the key points are the failure location, the failure mode, and the maximum sustained load only.

Tensile specimens for determining the mechanical properties along with direction 1 are produced flatwise, with their longitudinal direction aligned with direction  $X$  in the 3D printer reference system and a linear infill with a raster angle equal to  $0^\circ$ . Given its shape and mesostructure, such a specimen raises some questions. First, the infill filaments do not fully develop in the longitudinal direction in both configurations; some go through the entire length while others end on the filleted surface. The continuous filaments cooperate in load transmission along their length; however, high shear stresses might develop in the width-tapering region, especially on the contact surfaces between the last discontinued filaments and the first continuous filaments (moving from outside to inside). Second, the slicing software algorithm produces an asymmetric distribution of discontinued filaments. To conclude, at each end of the discontinued filaments, an edge corner appears.

Tensile specimens for determining the mechanical properties along with direction 2 are produced sidewise. Their longitudinal direction is aligned with direction  $X$  in the 3D printer reference system and a linear infill with a raster angle equal to  $90^\circ$ . Given its dog-bone shape, the specimen sticks to the building plate just in correspondence to the lateral surfaces of the expansion regions. This precludes contact between the narrow section and the building plate and imposes to distribute some supports below the cantilevered sections. The above considerations and the mesostructure of the specimen originate new questions. First, the surface in contact with the supports would not be perfectly flat and smooth, featuring an uneven distribution of partially isolated filaments in the first layers. Second, the filleted surface profiles developing along the  $Z$  direction in the 3D printer reference system would have a stair-step aspect due to the layer-by-layer nature of FFF.

Two sets of four specimens were printed and then tested to evaluate their mechanical response in a tensile test. Figure 2a shows the outcome of the tests along with direction 1; Figure 2b shows those along with direction 2. All the specimens manifested unacceptable failures; they were located within the gripping region or in the transition zone. The specimens failed in the range of 30 – 40 MPa when loaded along with direction 1; 20 – 30 MPa when loaded along with direction 2. Those values are much lower than what is discussed in the literature for 3D-printed PLA. There is no hint of plastic

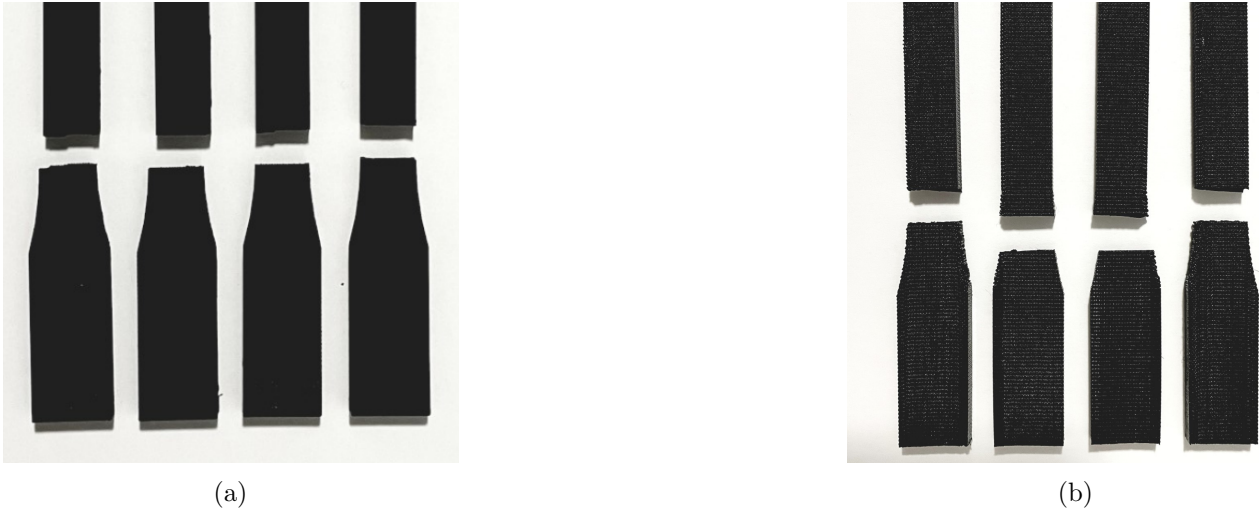


Figure 2: Failure modes of the dog-bone specimens in preliminary tests for determining the mechanical properties along with directions 1 (a) and 2 (b) in the material reference system. All the specimens manifested unacceptable failures since located inside the transition region.

deformation; all specimens failed with a clear fracture line. All these observations suggest that some stress concentration sources prematurely induced failures. Their location points to the conjunction between specimen geometry and mesostructures.

### 3.2 Tensile tests under ASTM D3039 guidelines

The tensile tests performed with the geometry provided for the polymeric materials did not lead to satisfactory results. As discussed, tensile tests along with directions 1 and 2 in the material reference system showed premature failures. Those failures have been justified with the conjunction between the specimen geometry and the two mesostructures. A distribution of defects has been identified across the transition zone, in which all failures occurred. Such geometry is therefore not suitable in this context. In the transition zones, the cross-section of the specimen changes. A solution is to test specimens featuring a constant section along the longitudinal axis not to induce any in-plane discontinuity. This guided the research activity towards the standard test method to determine tensile properties in composite materials, in which the cross-section is rectangular. The standardized test methods require a sufficient number of fibers within the cross-section to represent the feedstock material behavior statistically. The thickness and width of the specimens were increased with respect to the suggested values; this took into account the macroscopical difference between fiber and filament. The length was reduced to a value suiting the printing volume of most printers on the market, with a view to standardization. Table 3 reports a comparison between the recommended and the actual dimensions; W and T refer to the cross-section dimensions.

The ASTM standard suggests but does not require a set of 4 tabs for each specimen, two per end. They are interposed elements between the coupon and the gripping system, with three main features: being a thickness-tampering system aimed at supporting the specimen where a complex stress field exists; reducing the stress concentrations at the cross-section where the specimen comes off the grips; preventing specimen indentation.

#### 3.2.1 Tab design parameters

A careful definition of tabs is necessary. Their interposition between the specimen and the grips guarantees protection from superficial damages; however, their improper design might induce early failures

Dimensions [mm]	Recommended		Actual	
	0° ud.	90° ud.	TSD1	TSD2
LO - length overall	250	175	190	190
W - width	15	25	25	25
T - thickness	1	2	3	4

Table 3: Comparison between the dimensions of the tensile specimens recommended in ASTM D3039 and those used in the present work. The lengths suit the 3D printing build volume; width and thickness are higher to increase the number of filaments in the cross-section.

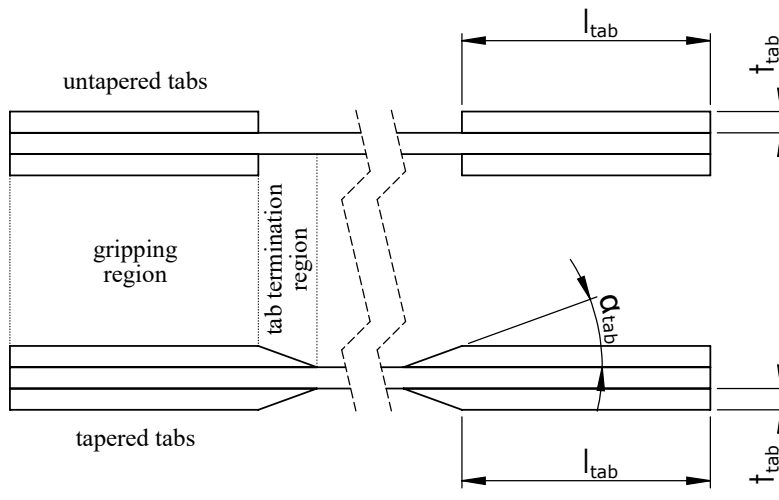


Figure 3: Untapered and tapered configurations of tabbed specimens for tensile properties determination provided for in ASTM D3039. The figure also defines the geometrical parameters of the tabs and identifies the so-called tab termination region.

themselves. The critical factors for an effective tab design are extensively discussed in the literature on composite materials [65], but their influence on FFF specimens needs experimental confirmation.

**Tab material.** It must adequately transfer the load to the specimen without failing/yielding beforehand. In composite materials testing, glass fiber composites and, more rarely, carbon/epoxy composites are used; metals are also considered in some applications. The material has been excluded from the variables; the experimental campaign relied on 3D-printed PLA tabs due to the following considerations. First, the *similarity in mechanical behavior*: using the same material for both the specimen and the tab allows speculating that no significant differences would arise. Second, the *customization*: the geometry and the dimensions can be easily and in real-time customized following the research outputs. Third, the *glue affinity*: the behavior of the adhesive is the same towards both the glued components, as their material is.

**The adhesive.** It transmits the load from the tabs to the specimen through shear stresses. Cyanoacrylate adhesives effectively bind PLA components; UHU Bostik two-component epoxy adhesive D2870 has been used, as it ranks among the commercial adhesives with the highest adhesive strengths, reporting 170 km/cm<sup>2</sup>.

**The geometry.** It plays a critical role in load transmission. Figure 3 describes two alternative geometries in a tabbed specimen differing in the termination region only, which can be either untapered or tapered. Untapered coupons feature a sudden shift between the region of interest and the gripping area; this is not the case with tapered specimens, highlighting a gradual transition. Three parameters

Factors		Levels			
$t_{tab}$ - Thickness	[mm]	0.5	1	1.5	2
$\alpha_{tab}$ - Taper angle	[deg]	5°	10°	20°	90°
$v$ - Test speed	[mm/min]	0.5	2	3.5	5

Table 4: Tab design: the table shows the factors and levels used for tensile and in-plane shear specimens. The research considered the test speed as a factor of the first DoE only.

adequately describe the tapered configuration: the *tab thickness*,  $t_{tab}$ , the *tab taper angle*,  $\alpha_{tab}$ , and the *tab length*,  $l_{tab}$ . When the taper angle equals 90°, the tapered configuration degenerates into the untapered one. Consequently, the second can be considered as an extension of the first. In composite materials, the longer the tab is, the lower the stress concentration effects; this is true for short tabs but minimal in the 25 – 150 mm range. Lengths beyond 50 mm would have been ineffective, as this is the longitudinal dimension of the gripping device;  $l_{tab} = 50$  mm represented a fixed value. The geometric discontinuity between the transition region and the region of interest is lowered with smaller taper angles; potentially, a null taper angle could be beneficial. In addition to being infeasible, however, it can induce delamination in the transition region, which is not subjected to gripping pressure. The design has been framed in the range 5° – 90°, giving more importance to lower values. The literature on composite materials suggests a thickness range of 1 – 2 mm for general use; the design extended this range by considering thicknesses as low as 0.5 mm.

### 3.2.2 Tabbing procedure

Sacrificial PLA spools have been used in tab production, with their principal and flat surface lying on the building plate. This surface has been roughened with sandpaper to increase adhesion to the specimen. An equal amount of resin and hardening agent is squeezed from the double-syringe blister of the adhesive into the mixing glass. A synthetic spatula helps to mix the two parts and to apply them to the sample surfaces. The operation is speedy due to the short processing time of the adhesive. Some preliminary tests showed that removing the excess in glue and leveling it in the termination region is essential to avoid delamination. A clamp system holds components in place for an hour in the face of a recommended curing time of 20 minutes.

### 3.3 Tab design validation

The previous section identified the thickness and the taper angle as the design parameters to investigate. A two-factors, four-levels, Design of Experiment (DoE) has been considered to assess their influence. The Taguchi method has been selected, as it allows studying and quantifying the impact of different factors over a critical output in terms of mean and variance. It is also a good choice for factors with discrete values. Table 4 shows the factors and the levels; a simplified approach to the problem has been considered highlighting only four possible levels for each variable.

DoEs have been used to design both types of tensile specimens (and, as discussed later, in-plane shear specimens) as there was no certainty about the behavior of different coupons. Each DoE has been performed two times to validate the consistency of its results. The test speed has been added as a third parameter in the first DoE of direction 1 to assess the influence of different load application speeds on PLA behavior. Its influence appeared to be independent of that of the geometric dimensions of the tabs; it was then kept constant, equal to the value suggested for polymers testing (5 mm/min) in ASTM D638. Such value differs from those suggested in ASTM D3039, but it allows keeping consistency with methods commonly used when studying polymeric materials. Each test relied on an L16 design with 16 different specimens. As for the output variable, two parameters might be considered:

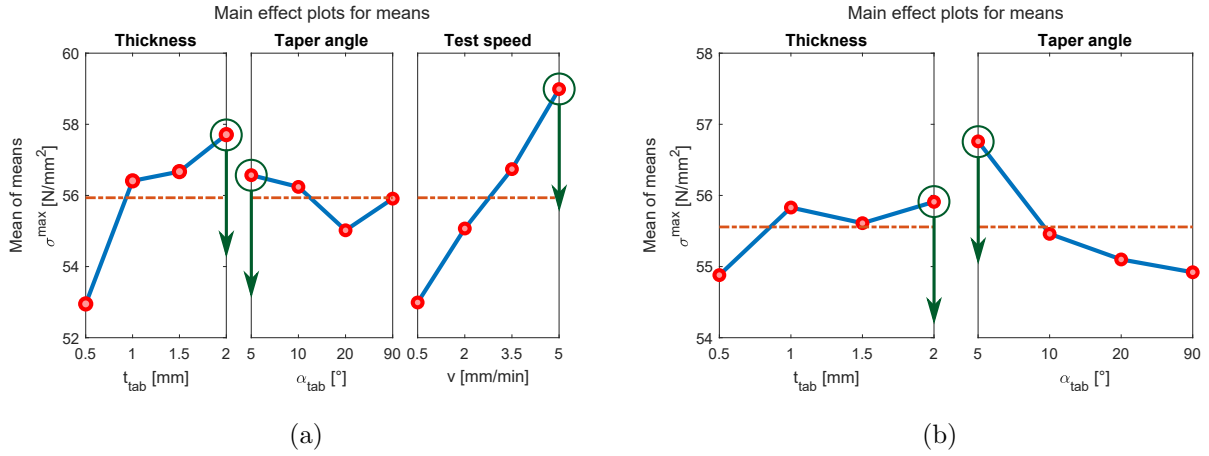


Figure 4: Tab design for tensile properties determination along with direction 1 in material reference system: results of the Taguchi analyses. The first analysis (a) shows the effects of  $t_{tab}$ ,  $\alpha_{tab}$ , and  $v$  on  $\sigma^{max}$ ; the second analysis (b) considers  $t_{tab}$  and  $\alpha_{tab}$  only. The results are consistent: in specimens loaded along with direction 1,  $\sigma^{max}$  is higher with low taper angles and high tab thickness. The effect of the testing speed can be distinguished from those of the geometrical parameters.

- *The maximum load,  $\sigma^{max}$ .* An inadequate tab geometry would induce a stress concentration, which allows speculating a premature failure/yield of the specimen.
- *The failure location,  $y^{fail}$ .* The specimen is expected to fail inside the region of interest, where the stress field should be uniform. A negative influence of a tab over the stress field would reflect on failure location. Specimens with different tab configurations feature other lengths for the region of interest. Thus, the measuring can be standardized, expressing the failure location into a percentage to the actual length of the specimen.

### 3.3.1 DoEs: specimens loaded in direction 1

Table 4 parameters, combined into an L16 design, gave 16 different combinations of tab thickness, tab bevel angle, and test speed for the first DoE; 16 different combinations of tab thickness and tab bevel angle for the second DoE. In the first run, acceptable failure modes (inside the region of interest) occurred three out of sixteen times; two further specimens failed at the limits of acceptability (the proximity of a tab). In the second run, five acceptable failure modes occurred, while two positioned at the boundaries. The proper load introduction has been evaluated in terms of the maximum load; the failure location could not be used due to the different residual deformations of the specimens. Figure 4a reports the results of the first DoE for specimens loaded along with direction 1; Figure 4b those of the second run.

The influence of the two geometrical parameters is coherent between the two runs:  $\sigma^{max}$  rises with the tab thickness and as the taper angle decreases. The first run also shows the influence of the testing speed on PLA behavior; the second run, however, confirms that its effect can be distinguished from those of the tab design parameters.

### 3.3.2 DoEs: specimens loaded in direction 2

The specimens loaded in direction 2 underwent the same process. Two DoEs with an L16 design verified the influence of the geometrical parameters of the tabs over the proper load introduction into the specimens. All specimens showed an initial linear behavior; however, they failed right after reaching

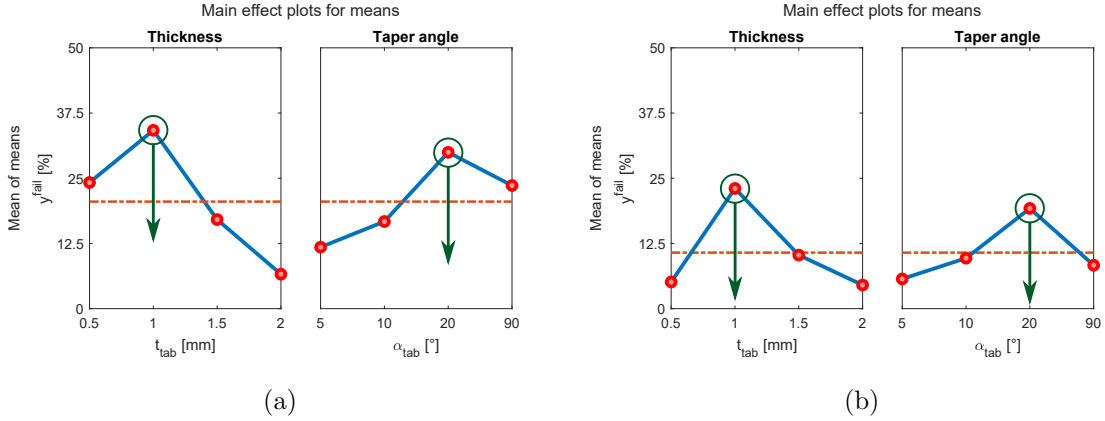


Figure 5: Tab design for tensile properties determination along with direction 2 in material reference system: results of the Taguchi analyses. The first analysis (a) and the second one (b) show the effects of  $t_{tab}$  and  $\alpha_{tab}$  on  $y^{fail}$ . The results are consistent: in specimens loaded along with direction 2, the failure location  $y^{fail}$  gets close to the coupon midsection with intermediate taper angle and tab thickness.

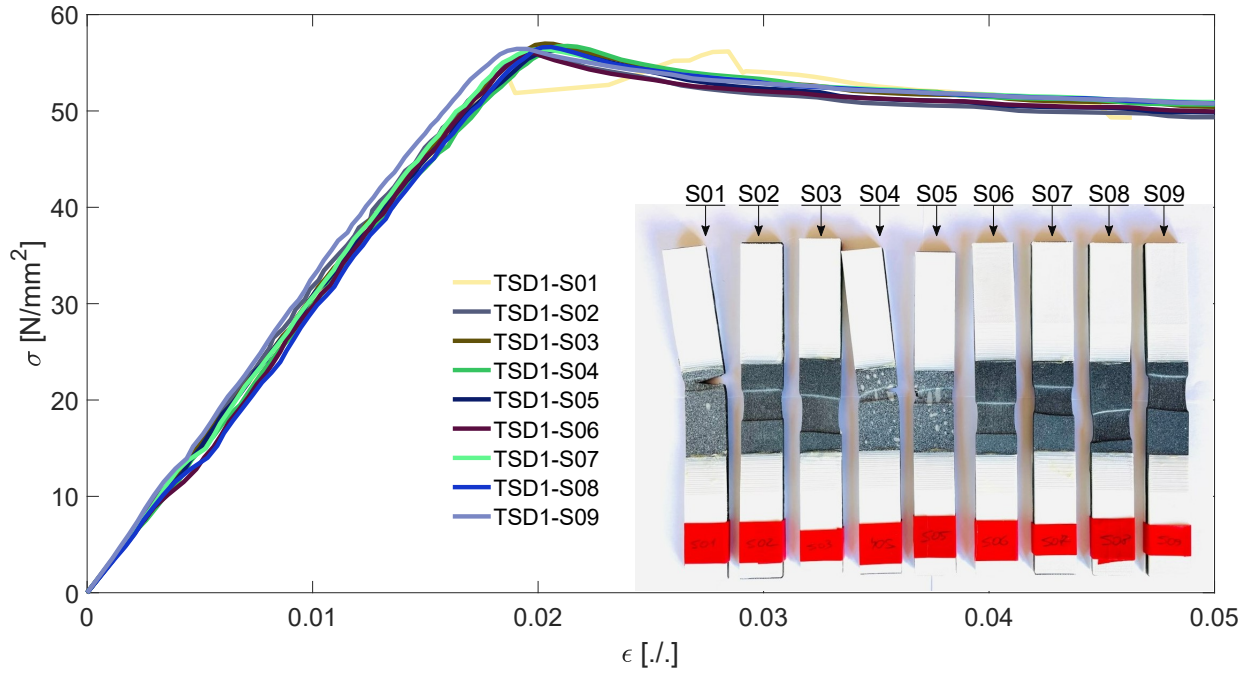
their highest sustained stress. In the first run, unacceptable failure modes occurred five out of sixteen times; most specimens failed in the gage section, although some near the termination region. In the second run, 11 out of 16 coupons showed an acceptable failure mode, even if most at boundaries. The failure mode variability is very low: a flat failure section characterized all specimens of both samples. At the same time, the maximum load is much less scattered throughout the samples, which prevented seizing precise results from the DoEs analysis. For this reason, the failure location  $y^{fail}$  has been considered as the output parameter. Measured from the nearest tab, it is indicated as a percentage of the length of the region of interest. This approach compensated for the different ROI lengths among the sample. The output improves as it comes closer to 50%, which represents the mid-section of each coupon. Figure 5a reports the results of the first DoE for specimens loaded along with direction 2; Figure 5b those of the second run; they show that a tab thickness of 1 mm and a taper angle of 20° drive the failure location towards the middle section of the specimen.

### 3.4 Tensile tests for mechanical characterization

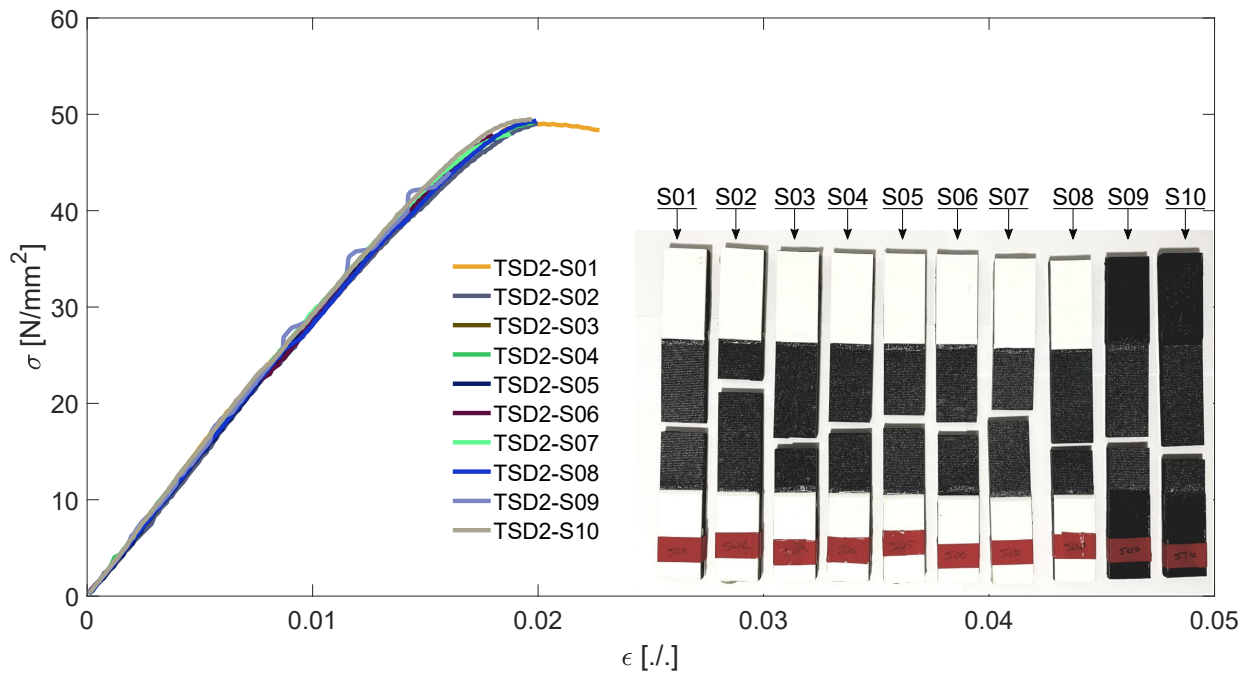
Choosing to use a single spool for mechanical characterization and validation tests limited the sample sizes to 10 specimens for directions 1 and 2, which is consistent with the ASTM D3039 requirements and preserves a margin for reprinting and retesting some coupons. From now on, Tensile Specimens will be indicated through the prefix *TS*, followed by the load application direction. For example, TSD1-S01 is the tensile specimen n°1 loaded along with direction 1.

The longitudinal stress vs. strain curves of the whole sample of specimens tested along with direction 1 are presented in Figure 6a, together with the failure modes. All coupons featured necking, and this took place inside the gauge section. The extensive plastic deformation altered the gray/white pattern, which prevented the DIC displacement correlation in the final stages of the tests; for this reason, the tests ended before rupture. Specimens 1, 4, and 5 confirm that they would have failed within the necked region. All the coupons behaved linearly in the early stages of the tests; the maximum sustained load is preceded by a slight divergence from linearity and followed by a broad plastic region at an approximately constant load.

The longitudinal stress vs. strain curves of the whole sample of specimens tested along with direction 2 are presented in Figure 6b, together with the failure modes. All coupons failed inside the gauge section, with an abrupt failure section coinciding with the interface among adjacent filaments. The absence of



(a)



(b)

Figure 6: Longitudinal stress vs. strain curves of the samples tested along with direction 1 (a) and direction 2 (b) in the material reference system. The figures also present the failed specimens, which all failed inside the gauge section: TSD1 specimens showed necking (a); TSD2 specimens showed an abrupt failure section (b).

SPECIMEN	Mechanical analysis				SPECIMEN	Mechanical analysis			
	$E_{11}$ [MPa]	$\sigma_{11}^{max}$ [MPa]	$\sigma_{11}^{pro}$ [MPa]	$\nu_{12}$ [-]		$E_{22}$ [MPa]	$\sigma_{22}^{max}$ [MPa]	$\sigma_{22}^{pro}$ [MPa]	$\nu_{23}$ [-]
TSD1-S01	3007	56.18	53.36	0.288	TSD2-S01	2863	49.03	47.74	0.282
TSD1-S02	3094	55.83	51.72	0.303	TSD2-S02	2783	49.03	46.24	0.233
TSD1-S03	3029	56.99	54.33	0.269	TSD2-S03	2902	46.79	46.60	0.265
TSD1-S04	2920	56.75	55.39	0.274	TSD2-S04	2905	49.10	46.22	0.289
TSD1-S05	2987	56.26	51.81	0.277	TSD2-S05	2866	47.66	47.16	0.252
TSD1-S06	2944	56.00	54.31	0.275	TSD2-S06	2840	47.90	47.31	0.249
TSD1-S07	3037	56.41	56.41	0.297	TSD2-S07	2902	48.01	43.88	0.286
TSD1-S08	2867	56.64	54.30	0.269	TSD2-S08	2821	49.36	46.47	0.262
TSD1-S09	3183	56.44	54.31	0.321	TSD2-S09	2950	44.03	43.54	0.259
TSD1-S10	—	—	—	—	TSD2-S10	2926	49.50	47.00	0.292
	TSD1 Sample					TSD2 Sample			
mean	<b>3008</b>	<b>56.39</b>	<b>53.99</b>	<b>0.286</b>	mean	<b>2876</b>	<b>48.04</b>	<b>46.22</b>	<b>0.267</b>
st.dev	94.51	0.368	1.522	0.018	st.dev	50.97	1.659	1.409	0.020

Table 5: Results of the experimental campaign on tensile specimens developed along with directions 1 (TSD1) and 2 (TSD2). The table reports the individual values of elastic modulus, tensile strength, tensile proportional limit, and Poisson ratio for each specimen. The last rows give the average values of the samples and their standard deviations.

macroscopic plastic deformation, and therefore of necking, is confirmed by the longitudinal stress vs. strain trend. All the coupons behaved linearly in the early stages of the tests; the maximum sustained load is preceded by a slight divergence from linearity and followed by a sudden failure.

By following the algorithm and procedures described in Section 2, the behavior of each specimen is described in Table 5 in terms of Young moduli  $E_{11}$  and  $E_{22}$ , tensile strengths  $\sigma_{11}^{max}$  and  $\sigma_{22}^{max}$ , tensile proportional limits  $\sigma_{11}^{pro}$  and  $\sigma_{22}^{pro}$ , and Poisson ratios  $\nu_{12}$  and  $\nu_{23}$ . The last line reports the mean values of these quantities, which will be considered the outputs of this characterization campaign, and the standard deviations.

## 4 Shear properties determination

This section is devoted to quantifying the in-plane shear mechanical properties. Once again, exploiting the parallel with unidirectional composites makes it possible to distinguish between in-plane shear behavior and interlaminar shear behavior. The literature reports several testing procedures, including: the V-notched/Iosipescu shear test, the rail shear test, and the V-notched rail method. All those tests feature a challenging setup, which is essential for interlaminar properties determination. In-plane shear modulus offers a simpler alternative. Specifically, ASTM D3518 describes how to determine the in-plane shear modulus of elasticity through a tensile test on  $\pm 45$  specimens; the peculiar lamination scheme of the coupon excites the shear response of the material. The parallel between fibers and filaments suggests that tensile specimens produced with an alternated raster angle of  $\pm 45$  might be used to complete the elastic coefficients matrix, determining the coefficient  $G_{12}$ . In ASTM D3518, the geometry of the coupon and the set-up of the test refer to ASTM D3039. The test method for composite materials requires a  $[+45/-45]_{ns}$  stacking sequence, with  $n$  between 4 and 6. The specimen thickness comes from the superposition of 16, 20, or 24 laminae. The macroscopical differences between fibers and filaments dimensions imposed a redesign; the number of layers was increased up to 30, implying a nominal thickness of 3 mm. The width was kept as suggested, and the overall length reduced to fit the

Dimensions		Recommended $\pm 45^\circ$ unid.	Actual SSD12
LO - length overall	[mm]	200 – 300	190
W - width	[mm]	25	25
T - thickness		16 – 20 – 24 laminae	3 mm

Table 6: Comparison between the dimensions of the in-plane shear specimens recommended in ASTM D3518 and those used in the present work. The lengths suit the 3D printing build volume; the thickness involves a stacking sequence of 30 layers, which increases the number of filaments in the cross-section.

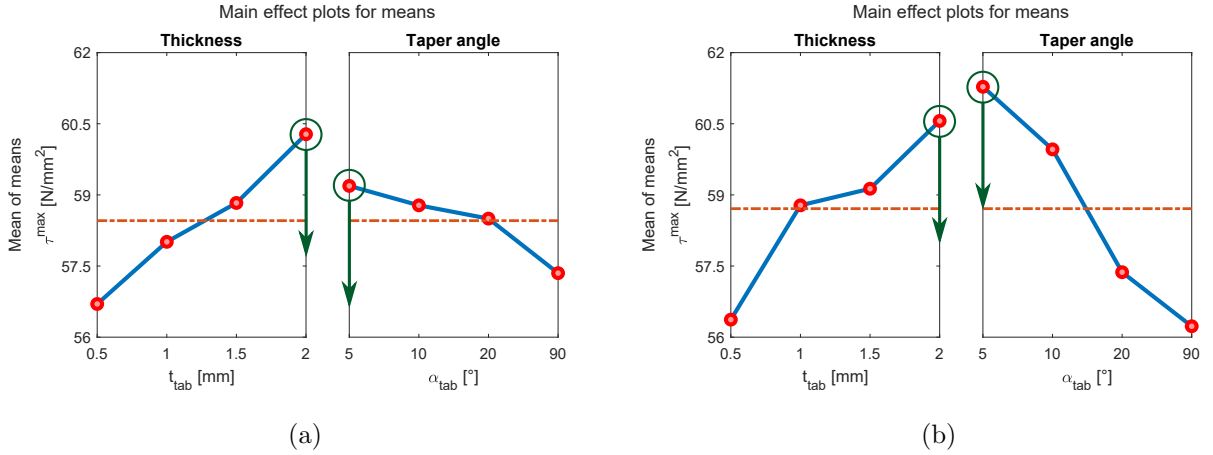


Figure 7: Tab design for in-plane shear properties determination: results of the Taguchi analyses. The first analysis (a) and the second analysis (b) show the effects of  $t_{tab}$  and  $\alpha_{tab}$  on  $\tau^{max}$ . The results are consistent: in specimens under shear stresses,  $\tau^{max}$  is higher with low taper angles and high tab thickness.

printing volume of most printers on the market. Table 6 compares the recommended and the actual dimensions of the specimens. As the only additional condition, the standard requires suspending the test if the coupon does not fail within the 5% strain limit. The main concern is the fiber (filament) scissoring that invalidates the original lamination. Tabs are usually not required; considering that this is, in essence, a tensile test, the same procedure described for tensile specimens assessment may be followed to define their significance (and characteristics).

#### 4.1 Tab design validation

The same argumentation for tensile tests still holds; as the tab and adhesive materials have been fixed, the validation of tab geometry follows the same path. A DoE allowed assessing the tab thickness and taper angle, combining the levels discussed in Table 4 into an L16 design. As in previous cases, the DoE was repeated twice to consolidate the results. The maximum sustained load varied considerably throughout the sample; almost all the coupons failed at  $45^\circ$ , strengthening the theory of near pure shear conditions. This forced using the maximum load sustained by the specimen,  $\tau^{max}$ , as the output parameter; the longitudinal distribution of the crack does not allow a coordinate to be associated with it. Few specimens of both the first and the second run failed outside the region of interest, suggesting the beneficial impact of the tabs. Figure 7a reports the results of the first DoE; Figure 7b those of the second run. The influence of the two geometrical parameters is evident in both the runs and similar to what happened for tensile specimens loaded in direction 1;  $\tau^{max}$  increases with the tab thickness and

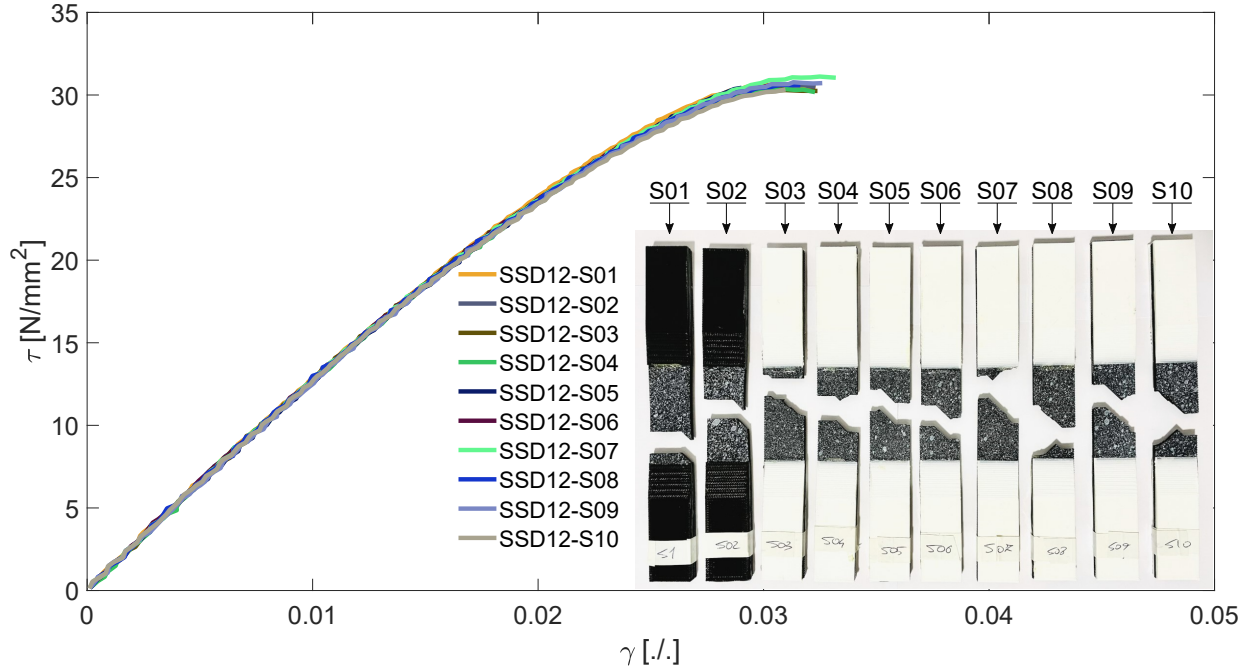


Figure 8: Shear stress vs. strain curves of the samples tested for determining the in-plane shear mechanical properties in the material reference system. The figures also present the failed specimens, which all failed inside the gauge section and showed an abrupt failure section parallel with one of the two filaments deposition directions.

as the taper angle decreases.

## 4.2 Shear tests under ASTM D3518

For the same reason discussed in Section 3.4, the sample size is limited to 10 coupons. The shear stress has been determined through Equation 6 using the applied load sampled by the testing machine; the shear strain is a consequence of the longitudinal and transverse strains, measured via DIC and calculated through Equation 7. From now on, Shear Specimens will be indicated through the prefix *SSD12*. For example, SSD12-S01 is the shear specimen n°1. The shear stress vs. strain curves of the whole sample of specimens are presented in Figure 8, together with the failed coupons.

The failure happened inside the gauge section in all coupons. Furthermore, the  $\pm 45^\circ$  failure section suggests shear stresses induced failure. All specimens showed the classic linear elastic behavior; a slight deviation from linearity preceded their failure, which occurred within the 5% strain limit. The Standard suggests a simplified method for calculating the stiffness modulus; a chord modulus quantified in a 4000  $\mu\epsilon$  range, starting from 4000  $\mu\epsilon$ . The results of the characterization campaign are shown in Table 7, in analogy with the previous cases.

## 5 CLT validation tests

The assumption that the anisotropy of 3D-printed PLA could be retraced to orthotropy under specific printing strategies guided the mechanical characterization campaign. The problem was then simplified by assuming that the Classical Lamination Theory could approximate the in-plane behavior, simplifying the characterization campaign to three tests and four mechanical quantities. The last point requires validation, which can be accomplished by exploiting CLT to simulate the mechanical behavior of 3D printed components under some experimental validation tests. This section discusses a three-point

SPECIMEN	Mechanical analysis	
	$G_{12}$ [MPa]	$\tau_{12}^{max}$ [MPa]
SSD12-S01	1232	30.63
SSD12-S02	1228	30.63
SSD12-S03	1240	30.30
SSD12-S04	1233	30.40
SSD12-S05	1213	30.65
SSD12-S06	1237	30.61
SSD12-S07	1230	31.12
SSD12-S08	1232	30.63
SSD12-S09	1206	30.77
SSD12-S10	1220	30.34
SSD12 Sample		
mean	<b>1227</b>	<b>30.61</b>
st.dev	10.81	0.236

Table 7: Results of the experimental campaign on in-plane shear specimens (SSD12). The table reports the individual values of shear modulus and shear strength for each specimen. The last rows give the average values of the samples and their standard deviations.

bending test, a bending, and a bending-torsion test on a cantilever beam with a point load at the tip, and simulates them through the Finite Element Method. Each test has been repeated with three different specimens in terms of raster angle to accentuate any difference among them, thus validating the non-isotropic behavior of 3D-printed PLA, and verify if PLA behavior can be predicted through CLT in different printing configurations. Each validation test has been simulated through Finite Element Analysis by considering two different constitutive models for 3D printed PLA:

**PLA(ORT)**: 2D linear elastic orthotropic, defined through the characterization campaign outputs of the previous section. The orthotropic behavior in FE shell elements is based on FSDT, characterized by a  $5 \times 5$  elastic coefficients matrix. However, shear penalization over  $G_{23}$  and  $G_{13}$  moduli allows retracing the constitutive model to CLT, which is characterized by a  $3 \times 3$  elastic coefficients matrix. The specimen thickness and configuration in terms of raster angle have been considered in the shell properties definition.

**PLA(ISO)**: 2D linear elastic isotropic model, defined through the mechanical properties declared by the manufacturer, assuming that 3D-printed PLA behaves isotropically even after the FFF process and despite how the printing parameters are set. The out-of-plane shear penalization was considered in this case also to keep consistency between the kinematics of the two.

The mechanical properties considered in the models are summarized in Table 8 for convenience.

## 5.1 Three-point bending test

The first test bench is a three-point bending test; it follows the guidance of the standard test methods for flexural properties determination in plastics, ASTM D790. An existent standard facilitates the set-up of the test and allows counting on existing testing supports. The specimen is a plate with a constant and rectangular cross-section. Two cylinders support the coupon from below. A third cylinder acts symmetrically on the upper surface of the specimen; while it moves downwards, it makes the coupon bend. The method does not have specific dimensions for the sample; however, some geometric relationships are suggested. Materials of a different nature in manufacturing and mechanical behavior

PLA(ISO)			PLA(ORT)		
$E_{11}$	3950	MPa	$E_{11}$	3008	MPa
$E_{22}$	3950	MPa	$E_{22}$	2876	MPa
$\nu_{12}$	0.3	-	$\nu_{12}$	0.286	-
$G_{12}$	1519	MPa	$G_{12}$	1227	MPa
$G_{23}$	$10^3$	GPa	$G_{23}$	$10^3$	GPa
$G_{31}$	$10^3$	GPa	$G_{31}$	$10^3$	GPa

Table 8: Summary of the mechanical properties considered in the constitutive models of FE analyses. PLA(ISO) relies on the isotropic coefficients supplied by the manufacturer; PLA(ORT) is based on the results of the experimental campaign.

Dimensions		
$LO_{3pb}$ - length overall	140	mm
$L_{3pb}$ - supports span	90	mm
$b$ - width	25	mm
$d$ - depth	4	mm

Table 9: Geometrical dimensions of 3-point bending test specimens, following the guidelines in ASTM D790.

are distinguished. As no details on FFF-processed plastic are mentioned, reference will be made to orthotropic materials. When the shear strength is lower than the tensile strength measured along with the longitudinal axis of the specimen, a span-to-dept ratio greater than 16 : 1 is advised. The results of the experimental campaign suggest this is the case; Table 9 shows the selected dimensions. Specimen length and support span guarantee sufficient overhang, which avoids slipping during the test.

The standard requires that the test be conducted at a constant deformation rate of the external fibers  $Z = 0.01$  mm/mm·min. This quantity translates into a constant translation speed for the upper cylinder, which can be calculated using the geometrical dimensions of the specimen.

$$R = \frac{ZL_{3pb}^2}{6d} = 3.375 \text{ mm/min} \quad (8)$$

The mechanical response of the coupons can be evaluated through the modulus of elasticity in bending  $E_B$ , the ratio between the flexural stress  $\sigma_f$  and strain  $\epsilon_f$  in the region where the linear dependence between those two variables still holds. Equation 9 allows quickly calculating its value, as it relies on the slope of the tangent to the linear region of the load vs. deflection curve  $m$ , which are normalized through the geometrical dimensions of the sample:

$$E_B = \frac{L_{3pb}^3 m}{4bd^3} \quad (9)$$

A careful determination of the geometrical dimensions is necessary; the support span  $L_{3pb}$  and the specimen depth  $d$  play a crucial role due to their cube power. The alignment jig described in ASTM D790 has been designed, printed, and used to deal with this issue. It features two parallel cylindrical sockets on the bottom, spaced  $L_{3pb} = 90$  mm. A third semi-cylindrical socket appears on the top surface; it is parallel to the former two and is positioned midway. The bottom sockets house the supporting cylinders of the testing machine; the top houses the loading nose. Used before each test, it checks that the alignment of all the cylinders, that the bottom supports have the proper spacing, and that the loading nose lies mid-way.

The sample counted on a total number of 18 components, printed in three configurations as a function of their raster angle: 6 specimens featured a raster angle of  $0^\circ$ , 6 an angle of  $90^\circ$ , and last 6 a criss-cross lamination sequence  $\pm 45^\circ$ . The raster angles are measured from the longitudinal axis of the specimen. From now on, 3-Point Bending test specimens will be indicated through the prefix *3PB*, followed by an indication of the specimen configuration. For example, 3PBD1-S01 is the 3-point bending test specimen n°1, in which the longitudinal axis is aligned with material direction 1 (the raster angle equals  $0^\circ$ ). A digital caliper helped evaluate the actual dimensions of the specimens; five measurements were taken per dimension, and the averaged values were considered. All tests have been performed through an Instron 8801 servo-hydraulic machine featuring a 1 kN load cell. The testing machine sampled the applied load and the centerline imposed deflection; those raw data can be respectively converted into flexural stress and strain by resorting to the following equations:

$$\sigma_f = \frac{3PL_{3pb}}{2bd^2} \quad , \quad \epsilon_f = \frac{6Dd}{L_{3pb}^2} \quad (10)$$

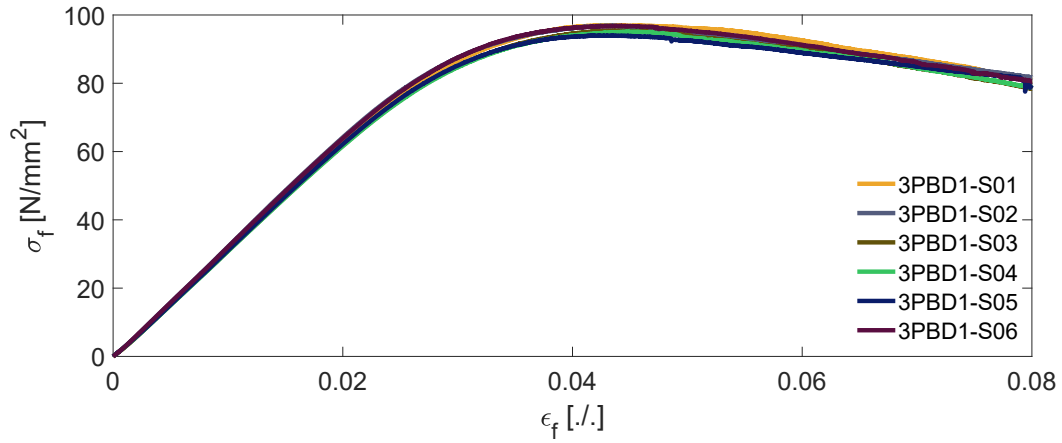
The flexural stress vs. strain relations are summarized in Figures 9a, 9b, and 9c for the three configurations. All the specimens exhibited an initial linear behavior, similar among those with the same configuration. A toe region precedes it due to the first instants of the test: before it begins, the upper cylinder and the specimen feature a small clearance to avoid undesirable preloading, but raw data sampling starts as soon as the testing machine is operated. This issue has been faced with zeroing loads and displacement recorded below 5 N. A more or less emphasized non-linear region appears after the initial linear one. The test method requires disregarding the response of the specimens over 5% strain due to the changed geometric configuration between the specimen and supports, which differs from simple bending. Both the linear region and the highest sustained load felt before this limit for each coupon; consequently, both the flexural modulus of elasticity and the flexural strength could be determined. The quantification of the first quantity followed the same algorithm described in Section 2.1 for tensile/in-plane shear modulus determination.

Figures 9a-9c show that the mechanical behavior depends on the configuration: 3PBD2 coupons suddenly failed at their maximum flexural load, which confirmed the brittle behavior along with direction 2. Instead, both 3PBD1 and 3PBD12 specimens showed a deviation from linearity before reaching their maximum load; after it, they manifested an extensive plastic behavior, reflecting that of tensile specimens.

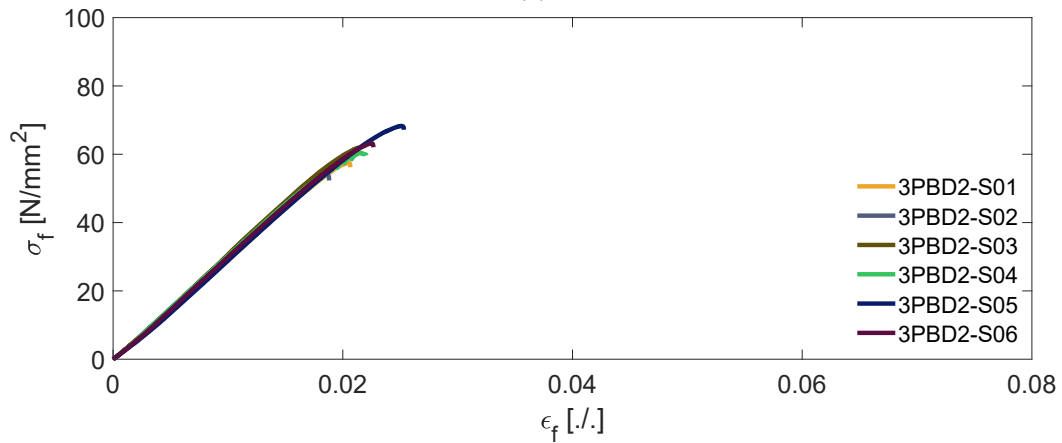
### 5.1.1 Finite element model

Setting up a FE model allowed recreating the specimen, the loading cylinders, and their kinematics. The boundary conditions replicate the experimental test: the lower cylinders act as constraints, and a displacement is imposed to the upper cylinder; this allows measuring the originating reaction forces. The cylinders are made of steel; they represent rigid and non-deformable bodies if compared to PLA coupons. They are three-dimensional components; their geometry is described through HEX elements, setting up a linear elastic constitutive model with  $E^{steel} = 210$  GPa and  $\nu^{steel} = 0.3$  as property values. A rectangle well describes the specimen geometry; two-dimensional CQUAD8 elements meshed it.

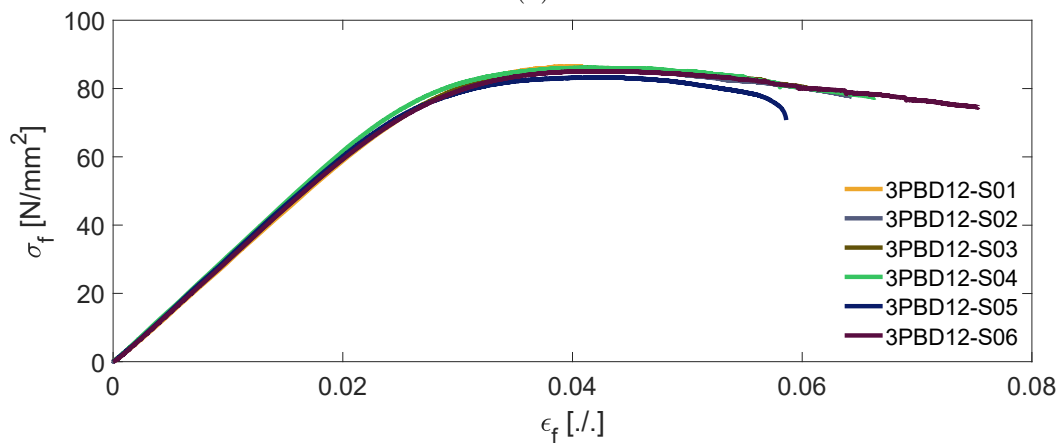
A non-zero friction coefficient avoids relative slipping while defining the contact relation between the cylinders and the specimen. The experimental measurement of the actual coefficient could not be performed; a set of preliminary analyses verified the impact of this parameter to exclude it could taint the outputs. Table 10 shows how the reaction force varied while increasing the friction coefficient  $\mu$  in the range  $0.005 - 0.7$ ; the specimen underwent 1 mm deflection at the midpoint. The reaction force keeps constant when some meaningless fluctuations at very low friction coefficients are excluded.  $\mu = 0.16 \pm 0.02$  is a value suggested in the literature for the contact between un-reinforced PLA and metals, and it is the value used with confidence in the present research.



(a)



(b)



(c)

Figure 9: Flexural stress vs. flexural strain curves of the samples tested in three-point validation tests. The figures report the outcomes of tests performed on specimens with filaments deposited along with the longitudinal direction, 3PBD1 (a), those of specimens with filament deposited along with the transverse direction, 3PBD2 (b), and those of specimens with criss-cross in-plane deposition, 3PBD12 (c).

Friction coeff. assessment		Mesh convergence		
Coefficient	Reaction Force	GEL	Reaction Force	Total strain energy
[./.]	[N]	[mm]	[N]	[10 <sup>-3</sup> J]
0.005	27.094	1	27.077	13.523
0.01	27.099	2	27.077	13.523
0.05	27.102	3	27.076	13.523
0.1	27.102	4	27.075	13.522
0.15	27.102	5	27.075	13.522
0.16	27.102	6	27.071	13.520
0.3	27.102	8	27.072	13.521
0.4	27.102	12.5	27.126	13.547
0.7	27.102	25	27.040	13.485

Table 10: Set-up of the FE model for the three-point bending test. The left columns evaluate the effect of the friction coefficient on the reaction force, which keeps constant, excluding some negligible fluctuations at very low coefficients. The right columns verify the performances of several meshes in terms of total strain energy and reaction force: a rapid convergence is observed. All the results consider a three-point bending test specimen under 1 mm deflection at mid-point.

The convergence of the mesh has been verified in terms of total strain energy and reaction force before finalizing the final model. Table 10 also shows their relations to the Global Edge Length (GEL), an averaged linear dimension of the elements. As in the previous background check, the specimen underwent 1 mm deflection at the midpoint. The results show a rapid convergence of the model; no practical difference exists in the outputs driven by 0.5 – 8 mm GELs. The fluctuations at high GELs and the gaps in its values derive from the size of the coupon;  $GEL = 25$  mm implies a single element in the transverse direction of the specimen,  $GEL = 12.5$  mm two. Thus,  $GEL = 8$  mm has been set. MSC Patran auto-mesher helped mesh the cylinders with HEX8 elements as they were not the main target of the analysis.

### 5.1.2 Experimental and numerical results comparison

This section aims to compare the experimental and the numerical results. Following the approach of the experimental tests, the model performances evaluation took place in terms of the equivalent modulus of elasticity in bending. It has been calculated through Equation 9, considering the imposed deflection and the resulting constraint forces. All the three raster angle configurations have been simulated. Table 11 compares the results. The experimental campaign confirms the anisotropy of 3D printed PLA: the behavior of the specimens depends on their configuration. The first one features the highest flexural modulus and flexural strength. By taking its modulus as a reference, the second and the third appeared to be less rigid at about 4% but showed similar results. PLA feedstock raw data denote inadequacy in describing its mechanical behavior; the percentage errors are in the order of 30%. They might represent the mechanical behavior of PLA pellets used in filament production and differ from those of the filament due to their production process and the specific additives. Beyond the numerical values of the isotropic coefficients, this constitutive model would be unsuitable in grasping the differences existing in the three configurations. Instead, the orthotropic model gives a precise description of the three laminations. No practical error arose in 3PBD1 and 3PBD2 configurations; FEM results almost coincide with those obtained from the experimental campaign. The gap is higher but still moderate for criss-cross lamination, which shows potential challenges in non-unidirectional laminations.

Exp.	3PBD1		3PBD2		3PBD12	
	$E_B = 3077$ MPa $\sigma_f^{max} = 95.84$ MPa		$E_B = 2953$ MPa $\sigma_f^{max} = 60.87$ MPa		$E_B = 2952$ MPa $\sigma_f^{max} = 85.46$ MPa	
PLA(ISO)	$E_B = 3995$	+29.8%	$E_B = 3995$	+35.3%	$E_B = 3995$	+35.4%
PLA(ORT)	<b><math>E_B = 3087</math></b>	<b>+0.3%</b>	<b><math>E_B = 2949</math></b>	<b>-0.1%</b>	<b><math>E_B = 3143</math></b>	<b>+6.5%</b>

Table 11: Comparison between experiments and simulations for the three-point bending tests (3PB) grouped depending on the filament deposition direction: longitudinally (3PBD1), transversally (3PBD2), and criss-cross  $[+45^\circ / -45^\circ]$  (3PBD12). The results are expressed in terms of bending moduli  $E_B$ . For the FE analyses, the constitutive model of PLA is reported on the left.

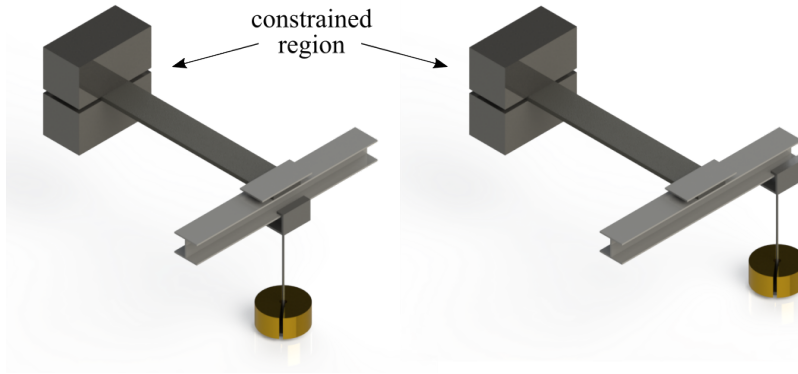


Figure 10: Graphic render of the simple bending and bending-torsion validation tests. A metal block constrains a rectangular coupon on its back; the H-beam on its front allows positioning a metal weight: when it lies in the middle, the specimen undergoes simple bending, otherwise, bending and torsion.

## 5.2 Bending and bending-torsion tests

This section proposes further validation tests with more structured boundary conditions than the three-point bending test. The experiments have then been replicated through a FE model by analogy to the previous case. Figure 10 presents a visual render of the setup; two configurations are possible, which allow performing two different tests. A rectangular coupon featuring a constant cross-section is constrained in its rear region with a metal block. The cross-sections dimensions are  $30 \times 4$  mm; the coupon is 190 mm in length, of which 50 mm are constrained. An H-beam is positioned at its front end; it acts as a slide: it allows loading the specimen with a metal weight and changing its position, which modifies the load case. When the load is in the middle, the coupon undergoes simple bending; otherwise, bending-torsion. Three coupons featuring the same configurations in the first test have been printed and tested in both the load case.

From now on, Constrained Simple Bending test specimens will be indicated through the prefix *CSB*, followed by an indication of the specimen configuration. For example, CSBD1 is the simple bending test specimen in which the longitudinal axis is aligned with material direction 1 (the raster angle equals  $0^\circ$ ). Constrained Bending-Torsion test specimens will be indicated through the prefix *CTB*, followed by an indication of the specimen configuration. For example, CTBD2 is the bending-torsion test specimen in which the longitudinal axis is aligned with material direction 2 (the raster angle equals  $90^\circ$ ). DIC has been considered to remotely monitor the front surface transverse displacements, which was prepared through an opaque white spray. The specimen vs. camera alignment has been checked through analog levels. Both the tests are not standardized; their characteristics have been precisely defined through preliminary evaluations.

The first concern is related to the loading. Manually adding the weight implies a dynamic action

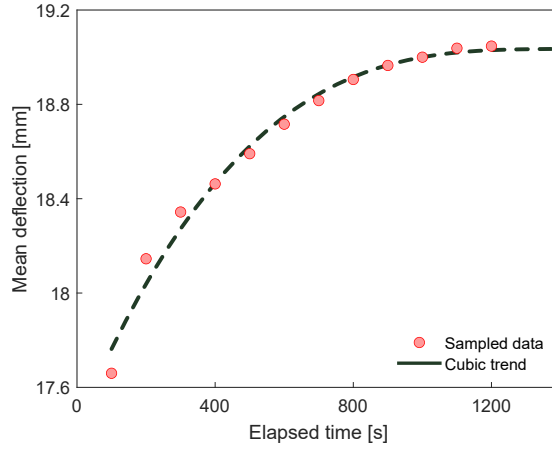


Figure 11: Preliminary evaluations on bending and bending-torsion tests set-ups. The figure evaluates how the mean deflection modifies over time in a simple bending test: the DIC experimentally sampled data show an asymptotic pattern from 1000 s forward.

occurring in a defined time interval: it is challenging to standardize/automate and causes oscillations. This issue might affect both the experimental and the numerical sides. DIC evaluates the displacements of each frame; this requires identifying a time interval to determine the effects under static conditions. This point is crucial also because the FE simulation will be static. A preliminary test assessed this point through the simple bending set-up for simplicity. 500 g is the applied load; DIC evaluated the displacements of the front surface in a time interval of 20 minutes, the maximum video length of the camera. The post-processing considered discrete intervals of 100 s, leading to 12 sampling instants. The mean surface deflection vs. time relation is provided in Figure 11. The deflection grows over time but shows an asymptotic pattern after 1000 s from load application. The more rigid response of plastics at high load application speed justifies this behavior: the coupon gradually adapts to the load and reaches a final equilibrium position. This led to identifying the static displacement as that recorded in the last frame of the video.

The second concern is related to the load amplitude. Once the point load is applied, the front surface will translate and rotate, losing its coplanarity with the undeformed configuration. Normal displacements to the original surface are a side effect of this rotation. The DIC set-up features a single camera with a fixed focal plane parallel to the original front surface of the coupon, which allows measuring the in-plane displacements only. However, the measurements could be tainted from the modified distance between the surface and the focal. A preliminary estimation of the front section displacement and rotation for different point loads at the tip was conducted, exploiting the Euler Bernoulli theory. This analysis assumed that the material is homogeneous, isotropic, and linear elastic behaving. Given the low elastic modulus of PLA and the geometrical dimensions of the specimen, substantial deflections and rotations resulted even by applying small loads. Therefore, tiny loads have been examined, choosing between laboratory tools. It has been considered to keep the front surface deflection lower than 4 mm and the rotation lower than  $4^\circ$ . All specimens underwent a total load of 200 g, split into a 100 g brass block and 100 g of supporting elements.

### 5.2.1 Finite element model

FE models have been designed to suit the experimental tests. Given the CLT approach, two-dimensional models were considered; the coupon description takes place through its mean surface. The same goes for the H-beam slide, described via its flanges and web. CQUAD4 shell elements establish the mesh of

Simple bending - CSBD1		
Experimental	PLA(ISO)	PLA(ORT)
$d_{end} = 3.85$ mm	$d_{end} = 2.83$ mm	$d_{end} = \mathbf{3.83}$ mm
–	–26.5%	– <b>0.5%</b>

Simple bending - CSBD2		
Experimental	PLA(ISO)	PLA(ORT)
$d_{end} = 3.99$ mm	$d_{end} = 2.83$ mm	$d_{end} = \mathbf{4.01}$ mm
–	–29.1%	+ <b>0.5%</b>

Simple bending - CSBD12		
Experimental	PLA(ISO)	PLA(ORT)
$d_{end} = 4.08$ mm	$d_{end} = 2.83$ mm	$d_{end} = \mathbf{3.77}$ mm
–	–30.6%	– <b>7.6%</b>

Table 12: Comparison between experiments and simulations for the simple bending tests (CSB) grouped depending on the filament deposition direction: longitudinally (CSBD1), transversally (CSBD2), and criss-cross  $[+45^\circ / -45^\circ]$  (CSBD12). The results are expressed in terms of tip deflection  $d_{end}$ . For the FE analyses, the constitutive model of PLA is reported on the left.

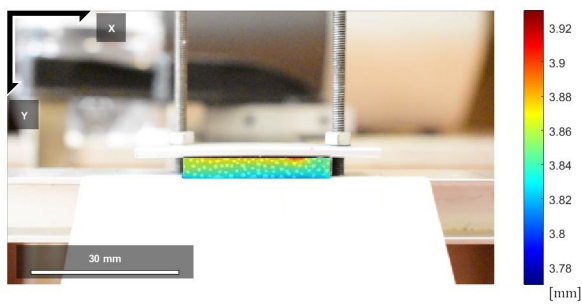
both components. The actual thicknesses of the components and an appropriate offset of the surfaces helped define a perfect bonding between the two parts. As with the three-point bending test cylinders, the H-beam is a rigid and non-deformable body compared to PLA. It featured a linear elastic isotropic constitutive model, considering  $E^{alu} = 73$  GPa and  $\nu^{alu} = 0.3$  as aluminium property values. The boundary conditions are described clearing all degrees of freedom in the constrained region. Two loads are applied. The first reflects the H-beam weight; it is fixed and applied in the vertical of the center of gravity. The H-beam is symmetric to the thickness-length plane of the specimen, so this load induces only bending. The second load is a further point load representing the brass block and its support. Its point of application depends on the load case: it is in the shear center of the cross-section, in the simple bending load case; it is at the end of the H-beam, in the bending-torsion load case.

### 5.2.2 Experimental and numerical results comparison

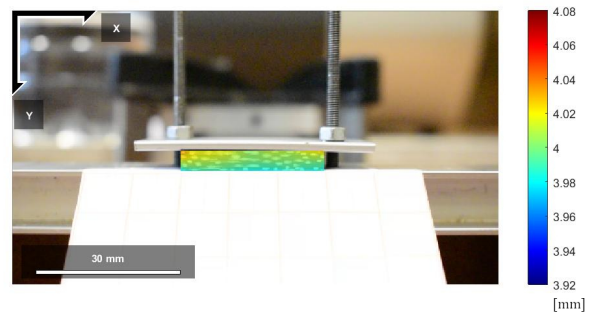
This section compares the experimental and the numerical results of the simple bending test and those of the bending-torsion test. When the specimen is constrained, and the H-beam fastened, the coupon is already slightly bent due to the metal slide weight in both tests. It acts as a 55 g weight in the middle. The DIC will monitor the effects of the further applied load of 145 g, which considers the 100 g brass block and its supporting elements. This further weight acts in the middle in simple bending tests; in the right endpoint in bending-torsion test. The same concept applies to the FE models, designed to evaluate the effects of the further 145 g load to the existing bending due to the H-beam weight.

Figures 12a-12c shows the DIC transverse displacements map of the specimens that underwent simple bending; they reflect the instant maps obtained after the time interval previously discussed to dissipate the loading-related vibrations. Table 12 discusses the experimental results of the simple bending tests in terms of end deflection  $d_{end}$  and compares them to the numerical outputs. The results consider the averaged transverse displacement of the end section as a representative measurement.

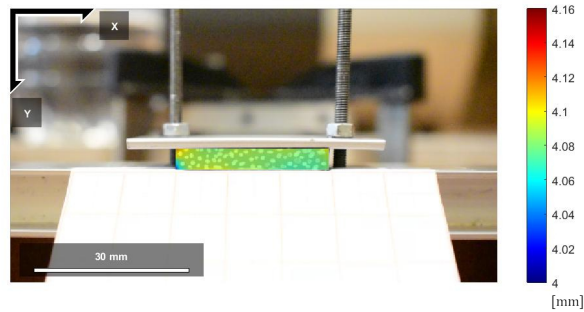
Figures 13a-13c show the DIC transverse displacements map of the specimens that underwent bending-torsion. As in the previous case, they reflect the instant maps obtained after the time interval previously discussed to dissipate the loading-related vibrations. Torsion induces a gradient in those maps; for this reason, the coupled effect of bending-torsion has been considered evaluating the



(a)



(b)



(c)

Figure 12: Simple bending tests: the figures show the DIC transverse displacement maps of the specimens with filaments deposited along with the longitudinal direction (CSBD1, a), along with the transverse direction (CSBD2, b), and with criss-cross in-plane deposition (CSBD12, c). A load of 145 g (brass block plus its supports) acts on the H-beam in the middle. The displacement maps are homogeneous, showing a constant displacement all over the front surface of the specimen, exception made for some boundary effects due to DIC.

Bending-torsion - CBTD1			
Experimental	PLA(ISO)		PLA(ORT)
$d_{end}^{LX} = 3.38$ mm	2.57 mm	-24%	<b>3.41</b> mm <b>+0.9%</b>
$d_{end}^{RX} = 4.38$ mm	3.26 mm	-26%	<b>4.25</b> mm <b>-3.0%</b>

Bending-torsion - CBTD2			
Experimental	PLA(ISO)		PLA(ORT)
$d_{end}^{LX} = 3.37$ mm	2.57 mm	-24%	<b>3.59</b> mm <b>+6.5%</b>
$d_{end}^{RX} = 4.31$ mm	3.26 mm	-24%	<b>4.43</b> mm <b>+2.8%</b>

Bending-torsion - CBTD12			
Experimental	PLA(ISO)		PLA(ORT)
$d_{end}^{LX} = 3.49$ mm	2.57 mm	-26%	<b>3.32</b> mm <b>-4.9%</b>
$d_{end}^{RX} = 4.47$ mm	3.26 mm	-27%	<b>4.21</b> mm <b>-5.8%</b>

Table 13: Comparison between experiments and simulations for the bending-torsion tests (CBT) grouped depending on the filament deposition direction: longitudinally (CBTD1), transversally (CBTD2), and criss-cross  $[+45^\circ / -45^\circ]$  (CBTD12). The results are expressed in terms of left  $d_{end}^{LX}$  and right  $d_{end}^{RX}$  tip deflection. For the FE analyses, the constitutive model of PLA is reported on the left.

transverse displacements at the right and left ends of the section. Table 13 discusses the experimental results of the bending-torsion tests in terms of end deflection at the right end  $d_{end}^{RX}$ , and at the left end  $d_{end}^{LX}$ , and compares them to the numerical outputs. Both analyses validate the deductions of the previous bending tests. PLA feedstock mechanical properties do not represent FFF-processed PLA. Therefore, prediction of the mechanical response of processed polymers is not possible through them. AA single result is the output, despite how the specimen has been printed; this implies that the isotropic constitutive model is wrong despite the specific values of the mechanical properties. The simple bending test is a simple load case in terms of boundary conditions and load application. The output of the orthotropic model follows the previous validation test: the error is almost zero in the CSBD1 and CSBD2 configurations; FEM results coincide with the experiments. A higher but still limited error appears in  $[\pm 45^\circ]$  raster angle configuration. Bending-torsion tests stress the structure more complexly, reflecting on more significant percentage deviations. However, the absolute values are minimal and lower than those attempted by the isotropic model.

## 6 Conclusions and future developments

This paper studied how FFF polymeric elements behave under defined processing and printing parameters. It demonstrated that a 100% linear infill reduces the anisotropy to a mild orthotropy. The authors defined a coherent setup for the mechanical characterization procedures, taking advantage of geometrical and behavioral similarities with unidirectional composites. Some of the approaches in the field were exploited and adapted for the experimental procedure. Investigating the in-plane behavior delivers a preliminary confirmation of these similarities; furthermore, it reduces the number of elastic coefficients to explore and extends the application of the Classical Lamination Theory to FFF.

A set of DoEs defined the influence of the tab geometry on how the load is introduced into tensile and in-plane shear specimens. The tensile coupons for determining the mechanical properties in the filament deposition direction and the in-plane shear coupons require thick tabs (2 mm) with a wide transition region (low taper angle,  $5^\circ$ ). On the contrary, the tensile specimens for quantifying the

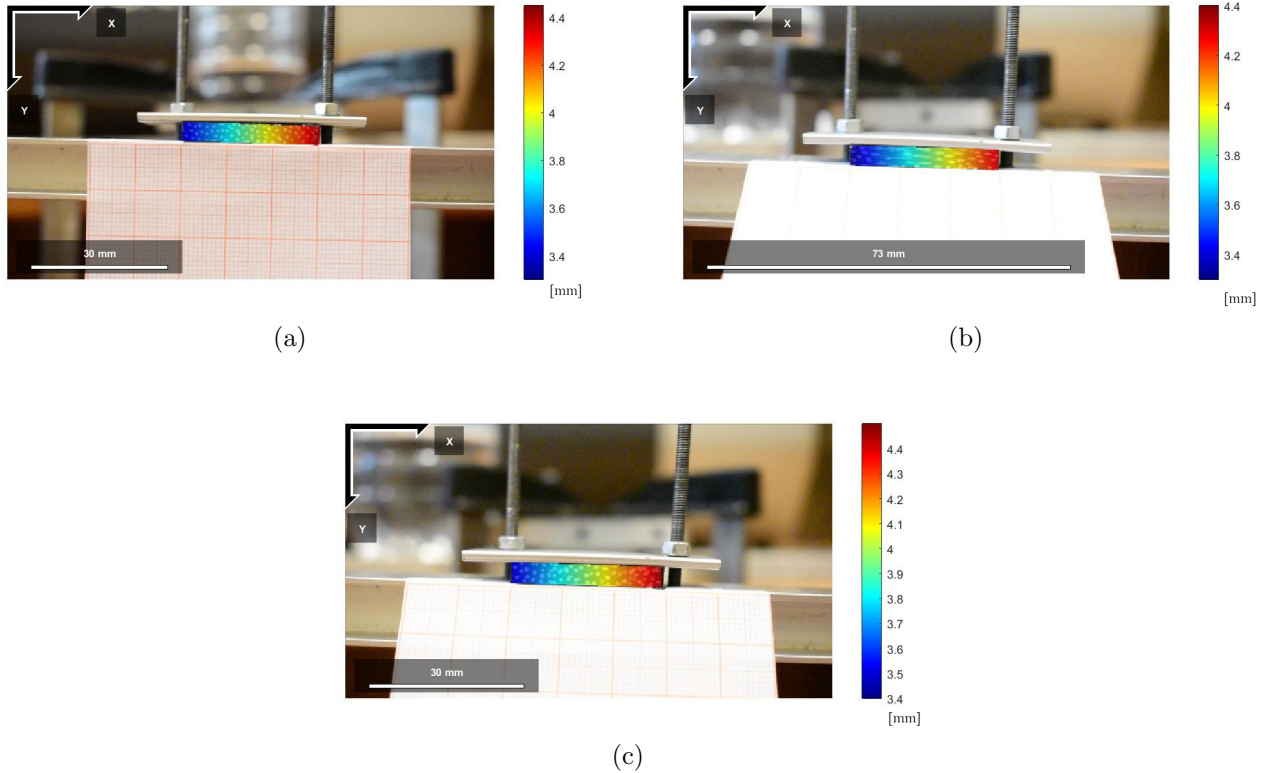


Figure 13: Bending-torsion tests: the figures show the DIC transverse displacement maps of the specimens with filaments deposited along with the longitudinal direction (CTBD1, a), along with the transverse direction (CTBD2, b), and with criss-cross in-plane deposition (CTBD12, c). A load of 145 g (brass block plus its supports) acts on the H-beam on its right end. The displacement maps show the displacement gradient due to torsion, which induces a cross-section rotation.

mechanical properties in the in-plane direction, which is orthogonal to the filaments, require thinner tabs (1 mm) with a high taper angle ( $20^\circ$ ). The results of the characterization campaign confirmed the anisotropy of the parts, which was relatively weak in terms of elastic moduli (3008 MPa vs. 2876 MPa, in directions 1 and 2, respectively), but more pronounced in terms of the ultimate tensile strength (54 MPa vs. 48 MPa, respectively).

The paper discussed a set of three-point bending tests and simple bending plus bending-torsion tests on a cantilever beam with a point load at the tip. The results on the specimens with different laminations further validated the non-isotropy. Finally, 2D FEMs simulated the validation tests with an orthotropic constitutive model based on CLT and tuned with the experimental mechanical properties. The numerical models returned excellent response predictions and framed the influence of the filament deposition directions. In modulus, the simulations returned errors included in the range 0.1 – 7.6%, which is an impressive result compared to errors as high as 30% obtained through the isotropic coefficients supplied by the manufacturer.

This paper has demonstrated that 2D FE models can lead to an excellent prediction of the mechanical response in thin components arranged in the build platform of the 3D-printer when tuned with the orthotropic constitutive model. Expanding this approach to the full  $6 \times 6$  elastic coefficient matrix will be the subject of subsequent work.

**Funding** This research did not receive any specific grant from funding agencies in the public, com-

mercial, or not-for-profit sectors.

## References

- [1] Z. Zhu, V.G. Dhokia, A. Nassehi, and S.T. Newman. A review of hybrid manufacturing processes – state of the art and future perspectives. *International Journal of Computer Integrated Manufacturing*, 26:596–615, 2013.
- [2] K.V. Wong and A. Hernandez. A review of additive manufacturing. *ISRN Mechanical Engineering*, 4:1–10, 2012.
- [3] A.E. Alexander, N. Wake, L. Chepelev, P. Brantner, J. Ryan, and K.C. Wang. A guideline for 3d printing terminology in biomedical research utilizing iso/astm standards. *3D Printing in Medicine*, 7:1–6, 2021.
- [4] J.P. Kruth, M.C. Leu, and T. Nakagawa. Progress in additive manufacturing and rapid prototyping. *CIRP Annals*, 47(2):525–540, 1998.
- [5] Y. Li, J. Guozhu, Y. Cheng, and Y. Hu. Bending and stretching of certain types of heterogeneous aeolotropic elastic plates. *International Journal of Production Research*, 55(5):1498–1515, 2017.
- [6] K. Liu and H. Lin. A study on the relationship between technical development and fundamental patents based on us granted patents. *European International Journal of Science and Technology*, 3:1–14, 2014.
- [7] V. Mazzanti, L. Malagutti, and F. Mollica. Fdm 3d printing of polymers containing natural fillers: A review of their mechanical properties. *Polymers*, 11(7):1–22, 2019.
- [8] A.M. Peterson. Review of acrylonitrile butadiene styrene in fused filament fabrication: A plastics engineering-focused perspective. *Additive Manufacturing*, 27:363–371, 2019.
- [9] M. Dwamena. *Which Layer Height is Best for 3D Printing?* 3dprinterly, 2020. <https://3dprinterly.com/which-layer-height-is-best-for-3d-printing/>. Accessed on October 1, 2020.
- [10] W. Zhu, X. Zhang, and D. Li. Flexible all-plastic aircraft models built by additive manufacturing for transonic wind tunnel tests. *Aerospace Science and Technology*, 84:237–244, 2018.
- [11] G.D. Goh, S. Agarwala, G.L. Goh, V. Dikshit, S. L. Sing, and W.Y. Yeong. Additive manufacturing in unmanned aerial vehicles (uavs): Challenges and potential. *Aerospace Science and Technology*, 63:140–151, 2017.
- [12] C.G. Ferro, S. Brischetto, R. Torre, and P. Maggiore. Characterization of abs specimens produced via the 3d printing technology for drone structural components. *Curved and Layered Structures*, 3:172–188, 2016.
- [13] J. Buhring, M. Nuno, and K.U. Schroder. Additive manufactured sandwich structures: Mechanical characterization and usage potential in small aircraft. *Aerospace Science and Technology*, 111:1–8, 2021.
- [14] R.T.L. Ferreira, I.C. Amatte, T.A. Dutra, and D. Bürger. Experimental characterization and micrography of 3d printed pla and pla reinforced with short carbon fibers. *Composites Part B: Engineering*, 124:88–100, 2017.

- [15] A.M. Seifans, S. Ayyagari, and M. Al-Haik. Elastic/viscoplastic characterization of additively manufactured composite based on continuous carbon fibers. *Aerospace Science and Technology*, 111:1–12, 2021.
- [16] G.D. Goh, W. Toh, Y.L. Yap, T.Y. Ng, and W.Y. Yeong. Additively manufactured continuous carbon fiber-reinforced thermoplastic for topology optimized unmanned aerial vehicle structures. *Composites Part B: Engineering*, 216:1–10, 2021.
- [17] O.A. Mohamed, S.H. Masood, and J.L Bhowmik. Optimization of fused deposition modeling process parameters: a review of current research and future prospects. *Journal of Materials Processing Technology*, 3:42–53, 2015.
- [18] A.M. Peterson. Review of acrylonitrile butadiene styrene in fused filament fabrication: A plastics engineering-focused perspective. *Additive Manufacturing*, 27:363–371, 2019.
- [19] C. Duty, J. Failla, S. Kim, J. Lindahl, B. Post, L. Love, and V. Kunc. Reducing mechanical anisotropy in extrusion-based printed parts. In *Proceedings of the 28th Annual International Solid Freeform Fabrication Symposium*.
- [20] M. Somireddy and A. Czekanski. Anisotropic material behavior of 3d printed composite structures – material extrusion additive manufacturing. *Materials & Design*, 195:1–12, 2020.
- [21] H.R. Dana, F. Barbe, L. Delbreilh, M. B. Azzouna, A. Guillet, and T. Breteau. Polymer additive manufacturing of ABS structure: Influence of printing direction on mechanical properties. *Journal of Manufacturing Processes*, 44, 2019.
- [22] V. Harshitha and S. S. Rao. Design and analysis of ISO standard bolt and nut in FDM 3D printer using PLA and ABS materials. *Materials Today: Proceedings*, 19(part 2).
- [23] J.F. Rodríguez, J.P. Thomas, and J.E. Renaud. Mechanical behavior of acrylonitrile butadiene styrene (abs) fused deposition materials. experimental investigation. *Rapid Prototyping Journal*, 7(3), 2001.
- [24] S.H. Ahn, M. Montero, D. Odell, S. Roundy, and Wright P.K. Anisotropic material properties of fused deposition modeling abs. *Rapid Prototyping Journal*, 8(4), 2002.
- [25] M. Lay, N.L.N. Thajudin, Z.A.A. Hamid, A. Rusli, M.K. Abdullah, and R.K. Shuib. Comparison of physical and mechanical properties of PLA, ABS and nylon 6 fabricated using fused deposition modeling and injection molding. *Composites Part B*, 176:1–8, 2019.
- [26] R.J. Zaldivar, D.B. Witkin, T. McLouth, D.N. Patel, K. Schmitt, and J.P. Nokes. Influence of processing and orientation print effects on the mechanical and thermal behavior of 3d-printed ultem®9085 material. *Additive Manufacturing*, 13, 2017.
- [27] A. W. Gebisa and H. G. Lemu. Influence of 3D Printing FDM Process Parameters on Tensile Property of ULTEM 9085. In *14th Global Congress of Manufacturing and Management (GCMM-2018)*. *Procedia Manufacturing* 30, pages 331–338. Elsevier, 2019.
- [28] I. Durgun and R. Ertan. Experimental investigation of fdm process for improvement of mechanical properties and production cost. *Rapid Prototyping Journal*, 20(3), 2014.
- [29] B. Wittbrodt and J.M. Pearce. The effects of pla color on material properties of 3-d printed components. *Additive Manufacturing*, 8:110–116, 2015.

- [30] J. Pu, C. McIlroy, A. Jones, and I. Ashcroft. Understanding mechanical properties in fused filament fabrication of polyether ether ketone. *Additive Manufacturing*, 37:1–9, 2021.
- [31] B.M. Tymrak, M. Kreiger, and J.M. Pearce. Mechanical properties of components fabricated with open-source 3-d printers under realistic environmental conditions. *Materials & Design*, 58:242–246, 2014.
- [32] M.S. Uddin, M.F.R. Sidek, M.A. Faizal, R. Ghomashchi, and A. Pramanik. Evaluating mechanical properties and failure mechanisms of fused deposition modeling acrylonitrile butadiene styrene parts. *Journal of Manufacturing Science and Engineering*, 139(8):242–246, 2017.
- [33] C.A. Griffiths, J. Howarth, G. de Almeida Rowbothamb, and A. Rees. Effect of build parameters on processing efficiency and material performance in fused deposition modelling. *The Second CIRP Conference on Biomanufacturing*, 49:28–32, 2016.
- [34] N.A. Bin Sukindar, M.K.A. Bin Mohd Ariffin, B.T.H.T. Bin Baharudin, C.A.B. Binti Jaafar, and M.I.S. Bin Ismail. Analysis on the impact process parameters on tensile strength using 3d printer repetier-host software. *Journal of Engineering and Applied Sciences*, 2017.
- [35] E. Cuan-Urquizo, E. Barocio, V. Tejada-Ortigoza, R.B. Pipes, C.A. Rodriguez, and A. Roman-Flores. Characterization of the mechanical properties of fff structures and materials: A review on the experimental, computational and theoretical approaches. *Materials*, 12, 2019.
- [36] A. Rodríguez-Panes, J. Claver, and A.M. Camach. The influence of manufacturing parameters on the mechanical behaviour of pla and abs pieces manufactured by fdm: A comparative analysis. *Materials*, 11, 2018.
- [37] G.C. Onwubolu and F. Rayegani. Characterization and optimization of mechanical properties of abs parts manufactured by the fused deposition modelling process. *International Journal of Manufacturing Engineering*, 2014.
- [38] M.S. Hossain, J. Ramos, M. Espalin, M. Perez, and R. Wicker. Improving tensile mechanical properties of fdm-manufactured specimens via modifying build parameters. In *Annual international solid freeform fabrication symposium*, 2013. ISSN: 1053-2153.
- [39] M.S. Hossain, M. Espalin, J. Ramos, M. Perez, and R. Wicker. Improved mechanical properties of fused deposition modeling-manufactured parts through build parameter modifications. *Polymer Testing*, 136(6), 2014.
- [40] C. Tang, J. Liu, Y. Yang, Y. Liu, S. Jiang, and W. Hao. Effect of process parameters on mechanical properties of 3d printed pla lattice structures. *Composites Part C: Open Access*, 3:1–15, 2020.
- [41] J. R. C. Dizon, A. H. Espera Jr, Q. Chen, and R. C. Advincula. Mechanical characterization of 3D-printed polymers. *Additive Manufacturing*, 20, 2018.
- [42] T. Letcher, B. Rankouhi, and S. Javadpour. Experimental study of mechanical properties of additively manufactured abs plastic as a function of layer parameters. In *Proceedings of the ASME 2015 International Mechanical Engineering Congress and Exposition*.
- [43] A.R. Torrado and D.A. Roberson. Failure analysis and anisotropy evaluation of 3d-printed tensile test specimens of different geometries and print raster patterns. *Journal of Failure Analysis and Prevention*, 16(1):154–166, 2016.
- [44] J.J. Laureto and J.M. Pearce. Anisotropic mechanical property variance between astm d638-14 type i and type iv fused filament fabricated specimens. *Polymer Testing*, 68:294–301, 2018.

- [45] M.D. Monzón, Z. Ortega, A. Martínez, and F. Ortega. Standardization in additive manufacturing: activities carried out by international organizations and projects. *The International Journal of Advanced Manufacturing Technology*, 76, 2014.
- [46] D. Kazmer. Three-dimensional printing of plastics. *The International Journal of Advanced Manufacturing Technology*, 2017.
- [47] R. Torre and S. Brischetto. Buckling developed in 3d printed pla cuboidal samples under compression: analytical, numerical and experimental investigations. *Additive Manufacturing*, 38:1–14, 2021.
- [48] S. Brischetto and R. Torre. Tensile and compressive behavior in the experimental tests for pla specimens produced via fused deposition modelling technique. *Journal of Composites Sciences*, 4:363–371, 2020.
- [49] C. Koch, L. Van Hulle, and N. Rudolph. Investigation of mechanical anisotropy of the fused filament fabrication process via customized tool path generation. *Additive Manufacturing*, 16:138–145, 2017.
- [50] J. Martínez, J.L. Diéguez, E. Ares, A. Pereira, P. Hernández, and J.A. Pérez. Comparative between fem models for fdm parts and their approach to a real mechanical behaviour. *Procedia Engineering*, 63:878–884, 2013.
- [51] M. Montero, S. Roundy, D. Odell, S.-H. Ahn, and P.K. Wright. Material characterization of fused deposition modeling (fdm) abs by designed experiments. In *Proceedings of Rapid Prototyping and Manufacturing Conference*, pages 1–21.
- [52] J.H. Yang, Z. Zhao, and S.H. Park. Evaluation of directional mechanical properties of 3d printed polymer parts. In *Proceedings of 15th International Conference on Control, Automation and Systems (ICCAS)*, pages 1952–1954.
- [53] P.K. Gurralla and S.P. Regalla. Part strength evolution with bonding between filaments in fused deposition modelling. *Virtual and Physical Prototyping*, 9(3):141–149, 2014.
- [54] L. Li, Q. Sun, C. Bellehumeur, and P. Gu. Composite modeling and analysis for fabrication of fdm prototypes with locally controlled properties. *Journal of Manufacturing Processes*, 4(2):252–264, 2002.
- [55] C. Casavola, A. Cazzato, V. Moramarco, and C. Pappalettere. Orthotropic mechanical properties of fused deposition modelling parts described by classical laminate theory. *Materials & Design*, 90:453–458, 2016.
- [56] Y.L. Yap, W. Toh, R. Koneru, Z.Y. Chua, K. Lin, K.M. Yeoh, C.M. Lim, J.S. Lee, N.A. Plemping, R. Lin, T.Y. Ng, K.I. Chan, H. Guang, W.Y.B. Chan, S.S. Teong, and G. Zheng. Finite element analysis of 3d-printed acrylonitrile styrene acrylate (asa) with ultrasonic material characterization. *International Journal of Computational Materials Science and Engineering*, 8:1–16, 2019.
- [57] Y.L. Yap, W. Toh, R. Koneru, K. Lin, K.M. Yeoh, C.M. Lim, J.S. Lee, N.A. Plemping, R. Lin, T.Y. Ng, K.I. Chan, H. Guang, W.Y.B. Chan, S.S. Teong, and G. Zheng. A non-destructive experimental-cum-numerical methodology for the characterization of 3d-printed materials—polycarbonate-acrylonitrile butadiene styrene (pc-abs). *Mechanics of Materials*, 132:121–133, 2019.

- [58] K. Saeed, A. McIlhagger, E. Harkin-Jones, J. Kelly, and E. Archer. Predication of the in-plane mechanical properties of continuous carbon fibre reinforced 3d printed polymer composites using classical laminated-plate theory. *Composite Structures*, 259:1–8, 2021.
- [59] Shenzhen Eryone Technology. *Eryone Galaxy PLA - Data Sheet*, 2019. [https://cdn-3d.niceshops.com/upload/file/Glitter\\_PLA\\_Filament\[2\].pdf](https://cdn-3d.niceshops.com/upload/file/Glitter_PLA_Filament[2].pdf).
- [60] Y. Yang, Y. Liu, W. Hao, G. Guo, and X. Cheng. Study on the fracture toughness of 3d printed engineering plastics. *Journal of Materials Engineering and Performance*, 1:1–7, 2021.
- [61] R. Torre and S. Brischetto. Reinforcing effect of strain gauges on 3d printed polymers: An experimental investigation. *American Journal of Engineering and Applied Sciences*, 14(1):7–24, 2021.
- [62] M.F. Beatty and S.W. Chewning. Numerical analysis of the reinforcement effect of a strain gage applied to a soft material. *International Journal of Engineering Science*, 17(7):907–915, 1979.
- [63] A. Ajovalasit, L. D’Acquisto, S. Fracapane, and B. Zuccarello. Stiffness and reinforcement effect of electrical resistance strain gauges. *Strain*, 43(4):299–305, 2007.
- [64] V. Bacovsky. *Review of Nikon 18-55mm f/3.5-5.6G DX optics*. Photographylife, 2020. <https://photographylife.com/reviews/nikon-18-55mm-dx-vr-af-p/2>. Accessed on October 1, 2020.
- [65] D.O. Adams and Adams D.F. *Tabbing guide for composite test specimens*. Federal Aviation Administration, Washington, 2002.